molecules

MDPI

*Review*

# Recent Progress in Metal Oxide-Based Photocatalysts for $CO_2$ Reduction to Solar Fuels: A Review

**Xuanzhen Li [1,†], Jing Xiong [1,2,†], Zhiling Tang [1], Wenjie He [1], Yingli Wang [1], Xiong Wang [1], Zhen Zhao [1] and Yuechang Wei [1,2,*]**

[1] State Key Laboratory of Heavy Oil Processing, College of Science, China University of Petroleum, Beijing 102249, China
[2] Key Laboratory of Optical Detection Technology for Oil and Gas, China University of Petroleum, Beijing 102249, China
* Correspondence: weiyc@cup.edu.cn
† These authors contributed equally to this work.

**Abstract:** One of the challenges in developing practical $CO_2$ photoconversion catalysts is the design of materials with a low cost, high activity and good stability. In this paper, excellent photocatalysts based on $TiO_2$, $WO_3$, ZnO, $Cu_2O$ and $CeO_2$ metal oxide materials, which are cost-effective, long-lasting, and easy to fabricate, are evaluated. The characteristics of the nanohybrid catalysts depend greatly on their architecture and design. Thus, we focus on outstanding materials that offer effective and practical solutions. Strategies to improve $CO_2$ conversion efficiency are summarized, including heterojunction, ion doping, defects, sensitization and morphology control, which can inspire the future improvement in photochemistry. The capacity of $CO_2$ adsorption is also pivotal, which varies with the morphological and electronic structures. Forms of 0D, 1D, 2D and 3DOM (zero/one/two-dimensional- and three-dimensional-ordered macroporous, respectively) are involved. Particularly, the several advantages of the 3DOM material make it an excellent candidate material for $CO_2$ conversion. Hence, we explain its preparation method. Based on the discussion, new insights and prospects for designing high-efficient metallic oxide photocatalysts to reduce $CO_2$ emissions are presented.

**Keywords:** photochemistry; $CO_2$ reduction; metal oxide materials; solar fuels; macroporous structure

check for updates

**Citation:** Li, X.; Xiong, J.; Tang, Z.; He, W.; Wang, Y.; Wang, X.; Zhao, Z.; Wei, Y. Recent Progress in Metal Oxide-Based Photocatalysts for $CO_2$ Reduction to Solar Fuels: A Review. *Molecules* **2023**, *28*, 1653. https://doi.org/10.3390/molecules28041653

Academic Editor: Sergio Navalon

Received: 22 December 2022
Revised: 30 January 2023
Accepted: 6 February 2023
Published: 9 February 2023



## 1. Introduction

According to the report from Carbon Emission Accounts and Datasets for emerging economies (CEADs), China has emitted more than 10 billion tons of $CO_2$ per year since 2018. It is inextricably linked to people's desire for a more comfortable and convenient life. Nearly 60% of total emissions emanated from the production of cement, steel and coal-fired power generation processes. As a result of the greenhouse effect caused by ever-growing $CO_2$, the global average temperature is continuously increasing [1] and various types of severe weather will incur more frequently, such as ice melting, land drought, typhoons, hurricanes, earthquakes and tsunamis [2]. It is, therefore, imperative to convert and utilize the $CO_2$ present in the atmosphere.

The transformation of $CO_2$ can be driven by illumination, electricity and heat [3]. Solar energy is a safe, clean, renewable and inexhaustible energy source, so it is ingenious to achieve this conversion with sunlight [4]. Additionally, the reaction conditions in photocatalytic processes are mild [5]; thus, it is easy to conduct experimental tests. A new world opened up since $H_2$ and $O_2$ were obtained after radiating $TiO_2$ with light. Extensive research about photocatalyst were conducted until the year of 2000. Since then, a growing number of materials have been designed and studied to absorb solar energy, including oxide semiconductors, sulfides (ZnS, CdS and $MoS_2$), and polyoxometalates ($Bi_2WO_6$, $Bi_2MoO_6$ and $BiFeO_3$) [6,7]. Organics, organometallic complexes, covalent organic

polymers and noncovalent self-assembled supramolecular organic matter are also involved. Among them, inorganic metal oxide materials are widely studied for establishing efficient artificial photosystems due to their low cost, facile synthesis, stable crystal structures and environmental friendliness. $TiO_2$, $Cu_2O$, ZnO, $WO_3$ and $CeO_2$ show promising research value as the most common materials.

Despite the significant progress that has been achieved, researchers still have difficulties in developing highly active catalysts because of poor light-harvesting capacity, low $CO_2$ adsorption capacity and rapid recombination of charge carriers. To this end, theoretical foundation and strategies to upgrade photocatalysts are described in detail in this article. Firstly, the advantages of exposed facets adjustment, and the morphology of 0D, 1D, 2D and 3DOM materials are summarized. Then, common co-catalyst materials are introduced. Defects, ion doping and sensitization engineering are also discussed. We provide a basic understanding on these approaches to inspire the future improvement in photocatalytic field. Furthermore, as inorganic metal oxide materials are more suitable for large-scale production, this paper can serve as a model for future industrialization.

## 2. Theoretical Foundation and Strategies of Photocatalytic $CO_2$ Reduction

The photocatalytic process in semiconductors can generally be described as shown in Figure 1. Upon being excited by an incident photon with energy equal to or higher than the bandgap (*Eg*), charge carriers are generated. Electrons ($e^-$) at the bottom of conduction band (CB) migrate to the surface of the catalyst to initiate reduction reactions with $CO_2$. Holes ($h^+$) at the top of valence band (VB) conduct oxidative reactions.

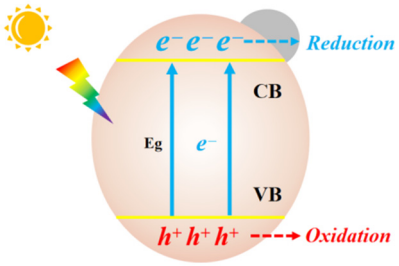


**Figure 1.** Fundamentals of photocatalytic reduction on a semiconductor catalyst.

The photocatalytic process of $CO_2$ conversion on semiconductors can be divided into five general steps: (1) Formation of electron–hole pairs under light radiation, (2) Separation and migration of the electrons and positive holes, (3) Adsorption and activation of $CO_2$, (4) Redox reactions that between surface-adsorbed species and electron–hole pairs, and (5) Desorption of the product. The electrochemical reactions with standard oxidation–reduction potentials (at pH 7 vs. NHE) are as follows:

$$H_2O + h^+ \rightarrow OH\bullet + H^+ \quad (1)$$

$$H^+ + e^- \rightarrow H\bullet \quad (2)$$

$$H\bullet + H\bullet \rightarrow H_2 \quad (3)$$

$$CO_2 + e^- \rightarrow CO_2^- \quad (4)$$

$$CO_2 + 2H^+ + 2e^- \rightarrow HCOOH,\ E_0 = -0.61\ V \quad (5)$$

$$CO_2 + 2H^+ + 2e^- \rightarrow CO + H_2O,\ E_0 = -0.53\ V \quad (6)$$

$$CO_2 + 4H^+ + 4e^- \rightarrow HCHO + H_2O,\ E_0 = -0.48\ V \quad (7)$$

$$CO_2 + 6H^+ + 6e^- \rightarrow CH_3OH + H_2O,\ E_0 = -0.38\ V \quad (8)$$

$$CO_2 + 8H^+ + 8e^- \rightarrow CH_4 + 2H_2O,\ E_0 = -0.24\ V \quad (9)$$

To carry out the conversion, it is necessary to comprehend the structure of $CO_2$. Due to the great symmetry and high bond energy of 750 kJ/mol, it is particularly difficult to break the C=O double bond. Therefore, the transmutation between $CO_2$ and bent radical anion of $CO_2^{\bullet-}$ on the surface of the catalyst is widely recognized as the first step to activate $CO_2$ for subsequent reaction. Additionally, photoreactions occur favorably only when the CB position of the catalyst presents a more negative potential than the target reduction and the VB position is more positive than the oxidation reaction. Figure 2A displays the $CO_2$ reduction potentials of some common semiconductors, along with the *E*g positions. From a molecular perspective, the adsorbed $CO_2$ is combined with $e^-$, $H^+$ or other intermediates on the surface of the catalyst. On the basis of newly-released reports, the photocatalytic mechanism of $CO_2$ reduction to $CH_4$/CO is graphically explained in Figure 2B [8–10].

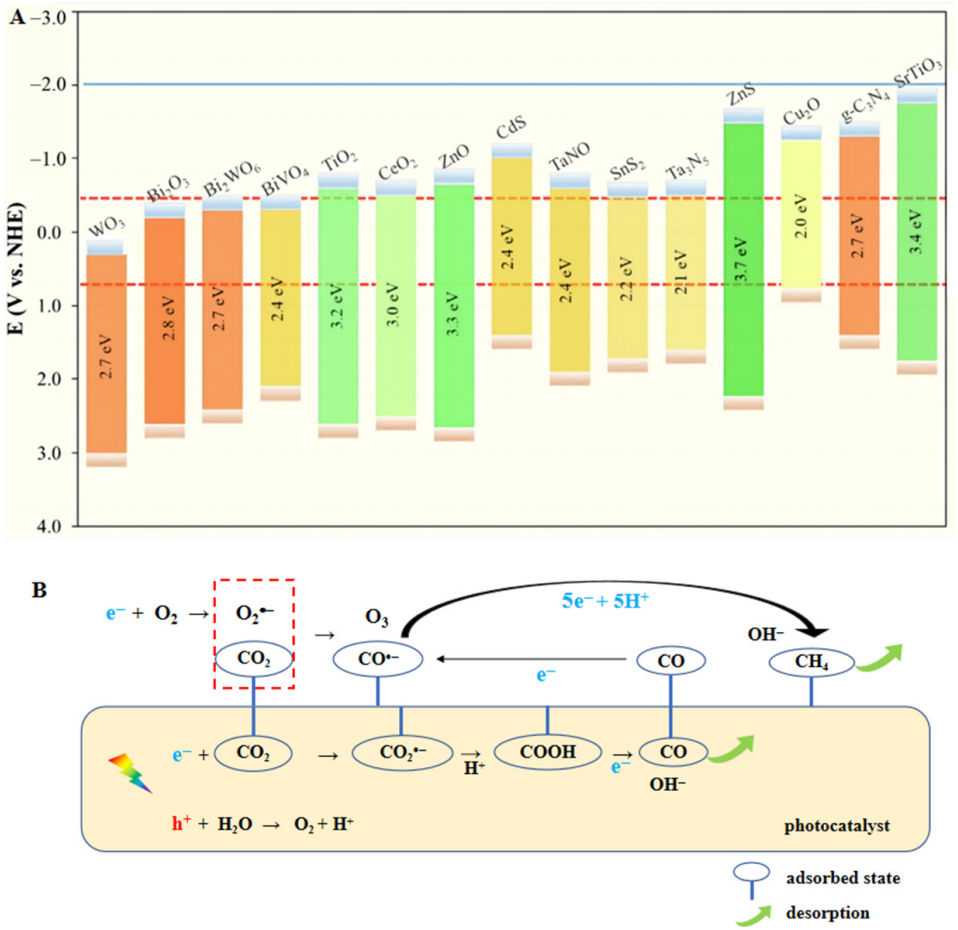


**Figure 2.** (**A**) Band edge positions of various semiconductors in relation to the redox potential of different products at pH = 7 [11]. (**B**) Schematic illustration of the mechanism for $CH_4$/CO generation.

Therefore, enough $e^-$ and $H^+$ are requisites for the entire photoreduction process. A series of fuels can be obtained by means of well-designed catalysts, such as $CH_4$ [12,13], $CH_3OH$ [14] and HCOOH [15]. It makes sense to create valuable solar fuel from $CO_2$, which provides a solution to environmental pollution. Products, alcohols, hydrocarbons and even carbon monoxide can be used as feedstock for energy reserves or high-value compounds.

Figure 3 summarizes the current strategies that can boost the photocatalytic $CO_2$ reduction pace, with detailed information being presented sequentially below.

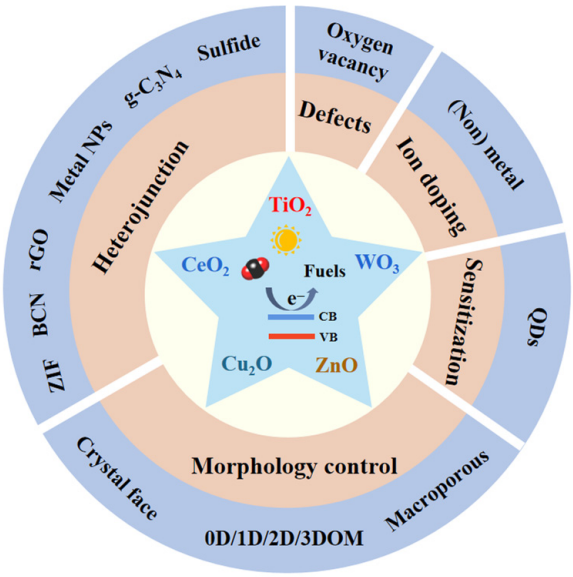


**Figure 3.** Strategies to boost the photocatalytic $CO_2$ reduction.

### *2.1. Morphology Control*

The surface topography of nanocrystals could evidently alter the electronic structure, surface energy and chemical properties of catalysts. Therefore, morphology control is one of the most important issues that concerns researchers in nanoscience, chemistry and physics. Open facets and edges determine the shape of nanocrystals. Thus, the preferential adsorption of additives on certain crystal surfaces provides a good opportunity to tune the surface of nanomaterials.

#### 2.1.1. Exposed Facet Adjustment

Exploring and figuring out the variation that is connected with exposed surfaces is crucial to elucidate shape-related chemical and physical properties. In semiconductor crystals, different facets have distinct electronic band structures that influence the transport of photoexcited carrier charges. It is wise to expose active facets to tune the $CO_2$ photoreduction efficiency [16].

#### 2.1.2. Quantum Dots (QDs)

Zero-dimensional (0D) semiconductor quantum dots (QDs) have many unique properties, such as quantum confinement effect, high extinction coefficient and multiple exciton generation [17]. Hence, QDs show much better photoactivity in the visible light region. Unlike bulk materials, surface atoms make up the majority of QD semiconductors. The abundant surface sites enhance the interaction between electron donors and acceptors, thus facilitating the photocatalytic charge transfer rate.

#### 2.1.3. One-Dimensional and Two-Dimensional Structures

One-dimensional nanostructured catalysts have high aspect ratios, such as nanowires, nanorods and nanotubes. The morphological tuning of the material makes a difference to their thermal, optical, electrical and magnetic properties [18]. For instance, the $TiO_2$ nanotube can act as a channel for electron transfer and build up the chemical reactions rate.

Two-dimensional layered materials can protect a tiny particle component from aggregating. The $CO_2$ adsorption capacity on the surface of 2D photocatalysts can be enhanced due to the large specific surface area and bountiful surface defects [19]. Two-dimensional lamellar nanosheets are widely used in photocatalysts, such as g-$C_3N_4$, $MoS_2$ and $WO_3$.

2.1.4. Macroporous and Three-Dimensional Ordered Macroporous (3DOM) Structures

Macroporous materials are being widely used in massive photocatalytic materials, owing to their excellent properties [20]. Unlike dispersed particles, sunlight can penetrate the pore wall easily and scatter widely inside the hollow structure, thus increasing the efficiency of illumination. Subsequently, the slender walls of pore reduce the transfer length of photo-generated charge carriers. Electrons ($e^-$) and holes ($h^+$) are separated more efficiently when heterojunctions are loaded on porous materials. The specific surface it provides is so large that more $CO_2$ molecules have a chance to contact the catalyst for reduction reactions.

Growing attention has been paid to hierarchical composite pores, including photonic crystal catalysis and separation of sub-microns. The slow light effect of photons associated with 3DOM materials have been considered to increase solar radiation absorption and enhance photocatalyst performance [21]. 3DOM products with periodic macrostructures [22], known as inverse opal, have been applied in battery materials, sensors, separation engineering and heterogeneous catalysis. Thanks to the periodic dielectric constants, Bragg diffraction permits certain wavelengths of light to radiate, leading to stop-band reflection. The limited photons reflected back will slow down at the edge of the stop bands, from which it received its name of "slow photons" [23,24]. It accelerates the light absorption rate when the photon energy is consistent with the absorption spectrum of the 3DOM materials [25]. In addition, the light scattering properties are optimized due to the relation between the macrospores and pore walls. For example, a 3D macro mesoporous Mo: $BiVO_4$ architecture [26] was designed and fabricated, which had a superior photocurrent density.

It has been demonstrated that gas absorption and separation functions benefit from orderly porous architectures [27]. 3DOM chemicals show superior $CO_2$ absorption/desorption rates than other commercial products, as the special structure can capture $CO_2$ from the ambient air by utilizing humidity variation. It is a great way to use microporous catalysts because it not only increases visible light absorption but also shortens the transport time of $CO_2$. They are available at a low cost through simple and rapid methods.

2.1.5. Preparation of 3DOM Materials

Specifically, 3DOM materials are produced by the colloidal crystal template (CCT) method (Figure 4). A uniform and close-connected organic sphere template can be obtained, firstly, through three key processes. Then, seep metallic salt sol into the void of microspheres. After heat treatment, the organic microsphere template fades away and leaves a metal oxide frame. (i) The polymerizable monomer (methyl methacrylate, styrene) and initiator are mixed and heated under the protection of Ar; (ii) the earlier reaction liquid is filtered with microfiltration membrane; (iii) the microsphere mixture is centrifuged at a high speed for a long time, yielding the polymethylmethacrylate (PMMA) or polystyrene (PS) template; (iv) the template is immersed in the precursor solution and (v) is calcinated.

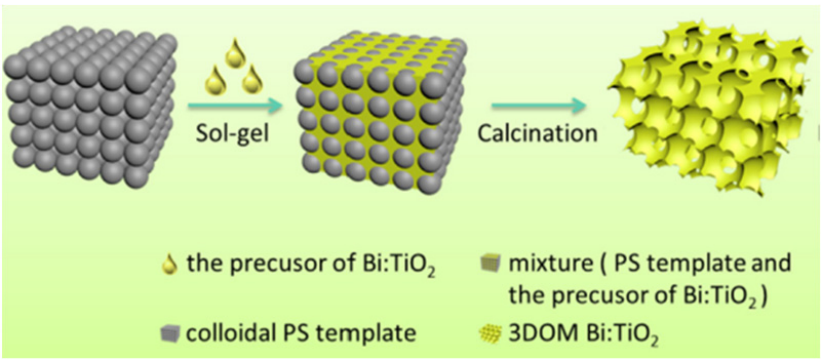


**Figure 4.** The fabrication process of the 3DOM Bi-doped $TiO_2$ [26].

In the absence of ultra-high temperature and expensive equipment, a fantastic 3DOM structure was obtained. Various materials of frame can also be synthesized by altering the precursor formula.

### *2.2. Heterojunction*

Photogenerated charge carriers in a single material tend to recombine rapidly due to coulombic force and they can be separated efficiently in the multi-materials that are in close contact [28]. The heterojunction is an interface between various semiconductors with different energy band structures. The heterojunction structure can reduce the probability of charge recombination and is therefore considered an effective method to enhance the photocatalytic activity [29,30].

### *2.3. Defects*

All semiconductors have surface defects, which are rooted in the absence of host atoms. The amount of oxygen vacancies can be altered by ion doping and nanocrystal modifications. Oxygen defects and other defects originating from the generated vacancy [31] can facilitate the separation of $h^+/e^-$. Over and above, defects can also activate $CO_2$ molecules, reducing the activation energy of the reaction [32].

### *2.4. Ion Doping*

Elemental doping is a common strategy to modulate the surface electronic structure. Then, the band gap of the semiconductors make a difference, nonmetal doping (such as N, C and O) mainly alters the VB and metal-doping (e.g., Mo, Co and Ni) influences the CB [33,34]. For example, Cu-doped $TiO_2$ absorbs more visible light due to the Cu 3d-Ti 3d optical transition [35].

### *2.5. Sensitization*

Sensitization means coupling the quantum dots, dyes, etc., with semiconductors to increase the photogenerated carriers and promote the absorption of light by taking advantage of their receptivity in UV, visible or infrared light.

In the following, exuberant measures to optimize $TiO_2$-, $WO_3$-, ZnO-, $Cu_2O$- and $CeO_2$-based photocatalysts for $CO_2$ reduction are demonstrated.

## 3. Photocatalysts with Different Basis Matrices

### *3.1. $TiO_2$-Based Photocatalysts*

Titanium dioxide ($TiO_2$) is notable in photochemistry, with advantages such as nontoxic, cheapness, corrosion resistant, good physical and chemical stability. However, owing to the wide *Eg* of 3.0–3.2 eV, $TiO_2$ only absorbs energy in the ultraviolet region (3–5% of the solar energy), and photoexcited charge pairs are easy to combine, resulting in quantum inefficiency. Usually, $TiO_2$ is divided into the rutile phase and anatase phase on the basis of atomic arrangement modes. Rutile $TiO_2$ is thermodynamically stable and does not distort or decompose at high temperatures. It has a narrower energy gap (3.0 eV) and a wider spectral response than the anatase phase (3.2 eV). Rutile $TiO_2$ seeds generally grow larger in size and tend to form an agglomerated structure. Smaller anatase $TiO_2$ particles have a wider lattice gap and abundant surface oxygen defects, which make it favorable for ion doping and photoreactions.

#### 3.1.1. Morphology Control

In hollow nanotube-shaped catalysts, the transport speed of $CO_2$ and photoproducts can be facilitated. Ru phase is inclined to form methane in $CO_2$ hydrogenation process [36] and Yang et al. [37] entrapped Ru nanoparticles in $TiO_2$ nanotubes. Restricted Ru nanoparticles were resistant to sintering and leaching in the Ru-in/TNT catalyst channel (Figure 5). Electrons tend to gather in the tubes because of a confinement effect, which leads to an

abundant, accessible metallic phase. It is easier for high-priced Ru species to combine with free electrons and then exhibit a superb $CH_4$ and $CH_3OH$ yield.

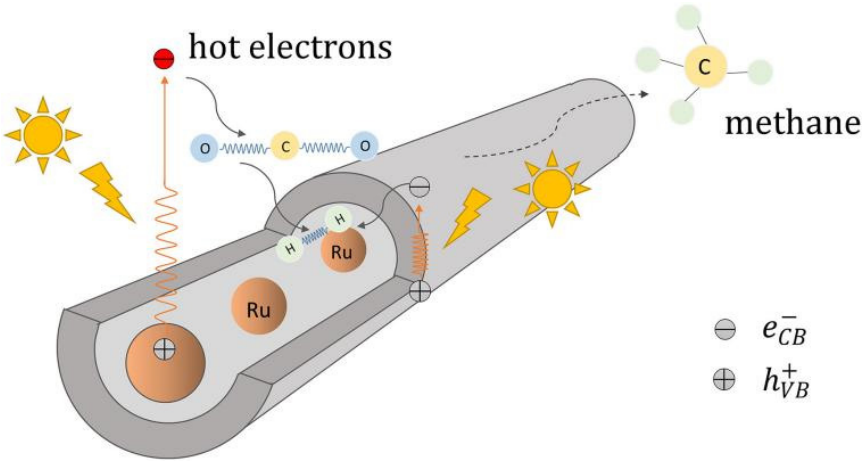


**Figure 5.** The reaction pathway for the Ru entrapped in the $TiO_2$ nanotubes catalyzes $CO_2$ methanation [37].

On the contrary, Kar et al. [38] loaded metal nanoparticles onto vertically oriented 1D $TiO_2$ nanotube arrays (TNAs) platforms via the graft method. In the synthesis process, Au, Ru and ZnPd NPs grow anodically on transparent glass substrates. There is no band bending phenomenon in Au NP-grafted $TiO_2$, which can be observed from ultraviolet photoelectron spectroscopy (UPS). TPD experiments proved that all NP-grafted samples absorb more $CO_2$ than TNAs. It is worth noting that, in nanoparticle-grafted TNAs, blue photons close to and below the $TiO_2$ band edge were excited to drive $CO_2$ photoreduction process. Ru-TNAs, ZnPd-TNAs and Au-TNAs had the $CH_4$ formation rates of 26, 27 and 58 $\mu mol \cdot g^{-1} \cdot h^{-1}$, respectively. Pt and $CoO_x$ growing on the outer and inner layers of a porous $TiO_2$-$SiO_2$ frame, respectively, can act as "warehouses" for $e^-$ and $h^+$, and the selectivity of the new system for reducing $CO_2$ to $CH_4$ can reach 94% [39].

Metal–organic frameworks (MOFs), also known as porous coordination polymers, composed of organic linkers and metal nodes (metal ions or clusters), are a kind of porous crystalline inorganic–organic hybrid materials. The unique advantages of MOFs, such as extremely high surface area, uniform adjustable porous structure and high density coordination unsaturated metal sites, have been extensively researched. They have been applied in many fields, such as gas adsorption and separation, sensing, catalysis, capture and conversion of $CO_2$. The high specific surface area and uniform porous structure of MOFs make it possible to incorporate metal nanoparticles (as electron acceptors) into their frameworks, leading to efficient charge separation. In addition, the eminent $CO_2$ adsorption capacity of various MOFs resulted in higher concentration of $CO_2$ in the pores, which helped to accelerate the photoreaction. In [40], a porous material-zirconium-based organic skeleton (UiO-66) was introduced to a $TiO_2$ photocatalyst as an effective $CO_2$ adsorbent. The designed two-step strategy endowed the $TiO_2$/UiO-66 composite with abundant graded pore structure, thus ensuring sufficient catalytic sites and high $CO_2$ adsorption capacity (78.9 $cm^3\ g^{-1}$). The ultrafine $TiO_2$ nanoparticles were loosely loaded on the UiO-66 surface rather than tightly packed due to the electrostatic repulsion, thus ensuring the exist of microporous of the MOF. Finally, in the weak gas–solid catalytic system with water as the electron donor, the yield of $CH_4$ was up to 17.9 $\mu mol\ g^{-1}\ h^{-1}$, and the selectivity was 90.4%. Additionally, the photocatalytic efficiency was comparable to that of pure $CO_2$ atmosphere even under low $CO_2$ concentration conditions ($\leq$2%).

Exposed Facet Adjustment

A Pt-$TiO_2$ single atomic site catalyst (PtSA/Def-s-$TiO_2$) was prepared [41] by the "thermal solvent-argon treatment and hydrogen reduction" method. In order to construct Ti–Pt–Ti structures, $TiO_2$ nanosheets with oxygen deficient sites were used to anchor monatomic Pt particles, which can retain the stability of isolated single atomic Pt and improve photocatalytic performance. The exposed (101) and (001) crystalline of $TiO_2$ nanosheets (Figure 6A,B) were determined by transmission electron microscopy, and a thickness of 6.9 nm was observed through atomic force microscope. The EPR spectra of the samples confirm that the rich oxygen defect structure can be obtained by heating $TiO_2$ nanosheets in argon atmosphere. They also indicated that single-atom Pt junctions were formed by occupying the oxygen defect sites, which provides a benchmark for the rational design of highly active and stable single-atom catalysts on metal oxide carriers with defect structures. $CH_4$ product can be detected when copper oxide nanoparticles are mixed with mesoporous $TiO_2$ nanorods in close contact [42]. Both the special crystal plane and porous structure contribute to furthering the $CH_4$ yield.

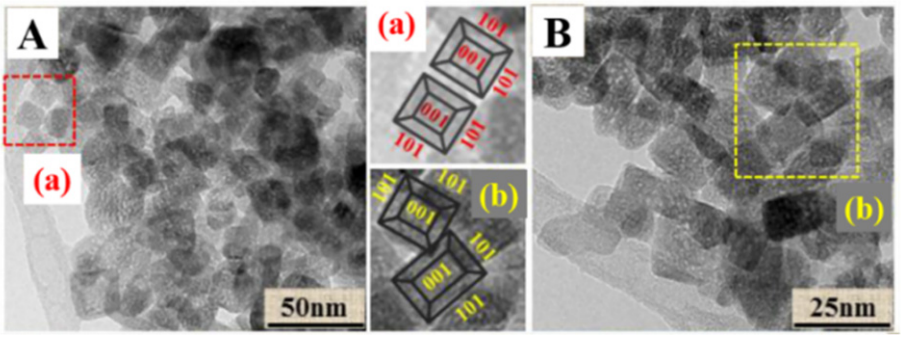


**Figure 6.** (**A**,**B**) HRTEM images of s-$TiO_2$ (**a**,**b**) partial enlarged drawing [41].

3DOM Structure Ti-Based Materials

A ternary 3DOM Bi-doped $TiO_2$ photocatalyst decorated with carbon dots (CDs) was obtained, whose pore engineering of the 3DOM skeleton greatly promoted the response in the whole solar spectrum range [26]. It exhibits enhanced photocatalytic performance because of its excellent exquisite structure and high charge transfer efficiency. Similarly, a $BiVO_4$/3DOM $TiO_2$ nanocomposite [43] was synthesized as a highly efficient photocatalytic catalyst for the degradation of dye pollutants. Further studies on its textural, optical and surface properties revealed that connecting pores not only improve the electron transfer rate between coupled materials, but also provide abundant active sites for reactant molecules.

3DOM $TiO_2$ were prepared [44] by the CCT method (Figure 7A) and $CeO_2$/3DOM $TiO_2$ samples (Figure 7B) were obtained by the original bubble-assisted membrane precipitation method. The introduction of $CeO_2$ nanolayers broadened the photo-absorption range and facilitated the separation of photogenerated electron−hole pairs. The mesoporous structure provided a larger surface area and the catalyst exhibited a higher $CO_2$ reduction activity.

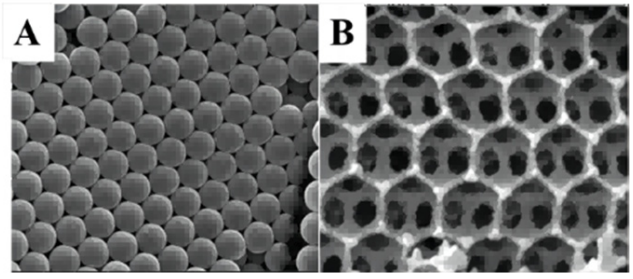


**Figure 7.** (**A**,**B**) SEM images of colloidal crystal template and $CeO_2$/3DOM $TiO_2$ [44].

Pt-particle-decorated 3DOM carbon-coated $TiO_2$ and g-$C_3N_4$ were combined [45] to construct an all-solid-state catalyst for $CO_2$ artificial photoconversion. Slow photon effect and carbon coat optimized the absorption capability of light. The exquisite design drove vectorial electrons from $TiO_2$@C to Pt particles and then fell to g-$C_3N_4$, which facilitated the carrier separation. The Z-scheme that consist of two isolated systems has three components and converts $CO_2$ to $CH_4$ with $H_2O$ at a yield of 65.6 μmol $g^{-1}$ $h^{-1}$. To enhance the surface enrichment of $CO_2$, Wu et al. [46] fabricated 3DOM perovskite-type $Pt_n/SrTiO_3$, in which Pt nanoparticles can take in photoelectrons from $SrTiO_3$ and transfer $CO_2$ to CO and $CH_4$ (Figure 8). $Pt_2$/3DOM $SrTiO_3$ exhibited the highest $CH_4$ yield of 26.7 μmol $g^{-1}$ $h^{-1}$.

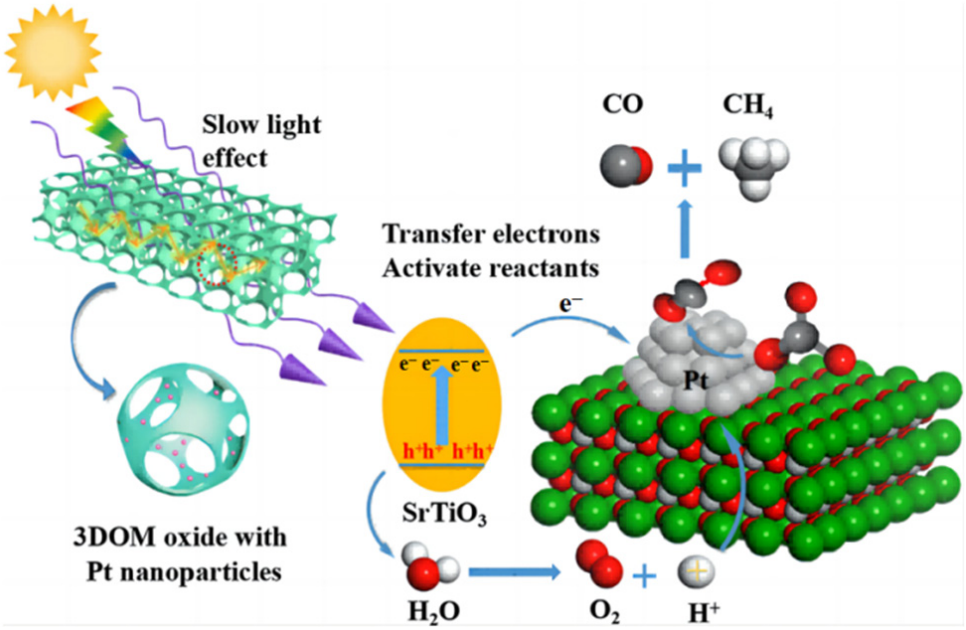


**Figure 8.** The possible mechanisms of the photocatalytic $CO_2$ reduction over Pt/3DOM $SrTiO_3$ [46].

A two-dimensional $MoS_2$ layers/3DOM $TiO_2$ photocatalyst was prepared [47] to form heterojunctions, which had a higher performance in the range of 420–900 nm. Cu single atoms were uniformly distributed in 3DOM $TiO_2$ via the in situ method [48], which provides active sites for $CO_2$ photoconversion. The main products tested in the gas–solid two-phase system were $CH_4$ and $C_2H_4$ with the corresponding generation rates of 43.15 and 6.99 μmol $g^{-1}$ $h^{-1}$. Chen's work provided a new perspective for improving the catalytic efficiency by regulating reaction conditions. Jiao et al. [49] loaded core-shell structure AuPd NPs in 3DOM $TiO_2$ via one pot of the gas bubbling-assisted membrane reduction method to form a functional photocatalyst. The low Fermi level of AuPd NPs empowered the catalyst system to trap electrons and enhance the separation of charge pairs. Carbon-quantum-dot-decorated 3DOM $CaTiO_3$ photocatalysts were duly obtained [50], exhibiting an apparent quantum efficiency (QAY). The macro–meso–microporosity structure provided improved charge carrier separation and transport, and it was explored in depth through density functional theory calculations (DFT) and finite difference time-domain simulations.

### 3.1.2. Heterojunction

p–n heterojunction: A p–n heterojunction is formed by combining p-type and n-type semiconductors. Even without light irradiation, electrons can diffuse from an n-type semiconductor to a nearby p-type one, in the case of the combination of two materials. Correspondingly, the holes on the surface of a p-type semiconductor are transferred to the n-type one, which results in an efficient separation of charge carriers. A $ZnFe_2O_4$-modified $TiO_2$ was synthesized by the hydrothermal method [51], and the p-n heterojunction system could reduce $CO_2$ to methanol at a yield of 75.34 μmol $g^{-1}$ $h^{-1}$.

rGO composite: In recent years, graphene materials have been widely used because of their large specific surface area, unique thermal stability and excellent electrical conductivity. Graphite nanomaterials are visible-light-responsive materials with appropriate band gaps, and the energy levels of CB and VB are in optimal positions relative to ordinary hydrogen electrodes. These unique photocatalytic properties have made them prime candidates for photocatalytic $CO_2$ reduction. Fortunately, tightly contacted ultra-thin graphene layers and $TiO_2$ compounds and can be prepared with some additives [52]. Seeharaj et al. [53] employed high-intensity ultrasonic waves (ultrasonic horn, 20 kHz, 150 W/cm$^2$) to exfoliate the $TiO_2$ surface, which led to a highly specific active area and highly reactive nanosheets. The modification of tiny rGO and $CeO_2$ on the rGO nanosheet surface can improve the $CO_2$ absorptivity and the charge carriers' migration efficiency of the catalyst (Figure 9). A kind of d–π electron orbital overlap was formed between $TiO_2$′s d orbitals and rGO's π orbitals, which provides a good environment for activated $CO_2$ and electrons. The complex heterojunction photocatalysts $TiO_2$/rGO/$CeO_2$ exhibited high yields of $CH_3OH$ (641 μmol/gcath) and $C_2H_5OH$ (271 μmol/gcath).

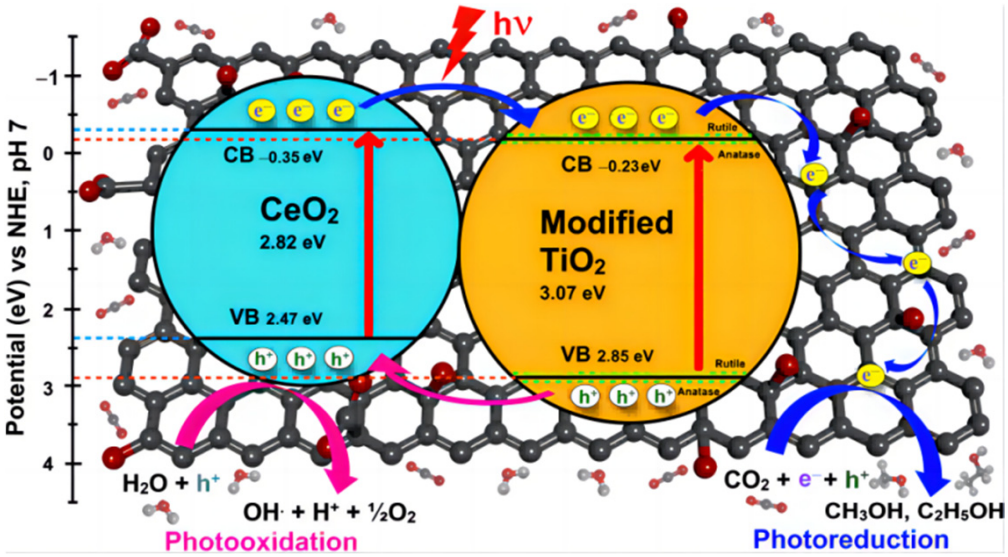


**Figure 9.** Mechanism for the photocatalytic conversion of $CO_2$ with $H_2O$ to methanol and ethanol over $TiO_2$/rGO/$CeO_2$ photocatalysts [53].

BCN composite: The boron carbon nitride (BCN) composite BCN is an adjustable band gap material that has been applied in $CO_2$ reduction, water splitting and as a detoxification catalyst. Highly negative CB potential of BCN materials makes them suitable for the construction of S-scheme heterojunction, and Kumar et al. [54] designed a novel S-scheme Fe@$TiO_2$/BCN composite. In situ XPS technology, DFT calculations and finite difference time-domain simulations were adopted to verify the S-scheme transfer mechanism. Under visible light irradiation, the intimately contacted heterojunction reduced the probability of charge recombination. The sample exhibited excellent photocatalytic activity; in addition to converting $CO_2$ selectively, it also degraded tetracycline antibiotics.

TMS composite: Some transition metal sulfides (TMSs) exhibit the same properties as Pt or Pd in photocatalyst. They form longer-lived charged carriers within the $S_{3p}$ orbital [55] with a highly negative reduction potential. However, the self-oxidation of metal sulfides confuses researchers and limits their application. It can be alleviated by constructing a Z-scheme, and thus researchers introduced it to Bi-modified $TiO_2$ [56]. Meanwhile, a spatially coupled heterojunction was enhanced by regularly capsulated $CuCo_2S_4$ yolk–shell hollow sphere.

#### 3.1.3. Ion Doping

In recent years, elements such as B, N, Co and Bi have been widely applied in $TiO_2$ doping. A carbon-based hybrid nanocomposite reduced graphene oxide (rGO), belonging to the narrow band gap, with oxygen-containing functional groups on the surface that can be enhanced by $\pi$ interactions [57]. Laminar graphene carriers not only prevent $TiO_2$ repolymerization, but also hybridize the function of the catalytic system. Co-doped $TiO_2$ was loaded on the rGO [58], and the Co peak in EDX spectra and C-O peak in FT-IR spectra confirmed the successful doping and the presence of graphene support, respectively. The size of $TiO_2$ particles decreased from 48–80 nm to 23–28 nm, which is consistent with earlier reports of changes in titanium doping with transition metal ions.

#### 3.1.4. Sensitization

A growing number of semiconductor materials are being used to modify $TiO_2$ dioxide, but randomly mixed catalysts are not stable enough to achieve reproducibility. Therefore, Lee [59] grew well dispersed p-type NiS nanoparticles on the surface of a highly aligned n-type $TiO_2$ film to obtain the NiS-sensitized $TiO_2$ films. The band gaps of two components were estimated by wavelength relation. Some inferences can be drawn when considering the results of both the ultraviolet and visible spectra. It indicates that more electrons are subpoenaed from the short-*E*g NiS and transferred to $TiO_2$ conduction band. The spectra results reconfirmed the electron contribution of the NiS and the design of a catalyst that produced 3.77-fold $CH_4$ compared to the $TiO_2$ film.

#### 3.1.5. Summary

Overall, some of the photocatalytic systems that use $TiO_2$ is presented in Table 1.

**Table 1.** Summary of the recent results of the photoreduction of $CO_2$ using $TiO_2$-based materials.

| Type of Enhancement | Photocatalyst | Description | Conditions (Lamp, Cutoff Filter) | Product Yield/ $\mu mol \cdot g^{-1} \cdot h^{-1}$ | Refs. |
|---|---|---|---|---|---|
| Heterojunction | Ag-NPs/$TiO_2$ | Core/shell | 200 W Hg | CO 983<br>$CH_4$ 9.73 | [60] |
| Z-scheme | $CuCo_2S_4$@3B-$TiO_2$ | CCS yolk–shell hollow spheres, Bi-modified $TiO_2$ | 300 W Xe | CO 25.5<br>$CH_4$ 42.2 | [56] |
| | Ag-$Cu_2O$/$TiO_2$ | P25 | | CO 13.19<br>$CH_4$ 1.74 | [61] |
| S-scheme | Fe@$TiO_2$/BCN | Fe@$TiO_2$/Boron Carbon nitride | 300 W Xe<br>400 nm | $CH_4$ 24.7 | [54] |
| p–n heterojunction | $ZnFe_2O_4$/$TiO_2$ | Spherical and irregular shapes | 500 W Xe | $CH_3OH$ 75.34 | [51] |
| Ion doping | Co-doped $TiO_2$/rGO | Equiaxed grain morphologies | 500 W Xe | $CH_3OH$ 133.7 | [58] |
| 3DOM | 3DOM Pt@CdS/$TiO_2$ | | 420 nm irradiation light, UV cutoff filter | $CH_4$ 36.8 | [62] |
| | AuPd/3DOM-$TiO_2$ | | 300 W Xe | $CH_4$ 18.5 | [28] |
| | $Pt_2$/3DOM-$SrTiO_3$ | | 300 W Xe | $CH_4$ 26.7 | [46] |
| | g-$C_3N_4$/Pt/3DOM $TiO_2$@C | | 300 W Xe<br>420 nm | $CH_4$ 65.6 | [45] |
| | $SnS_2$/3DOM $SrTiO_3$ | | 300 W Xe<br>420 nm | $CH_4$ 12.5 | [63] |
| | $Cu_{0.01}$/3DOM $TiO_2$ | | Xe (320–780 nm) | $CH_4$ 43.5 | [48] |
| | $MoS_2$/3DOM $TiO_2$ | | 300 W Xe<br>420 nm | $CH_4$ 11.6 | [47] |
| | 3DOM $CeO_2$/$TiO_2$ | | 300 W Xe<br>420 nm | CO 3.73 | [21] |

### *3.2. $WO_3$-Based Photocatalysts*

Tungsten-based oxides ($WO_3$) have been extensively studied in recent decades and various morphologies have been presented. In the $WO_3$ structure, the crystal in the stoichiometric ratio is connected with a twisted $WO_6$ octahedra to form a perovskite crystal structure. It has monoclinic, orthorhombic and hexagonal crystal forms. At the same time, the oxygen lattice can be lost easily, resulting in oxygen vacancies and unsaturated, coordinated W atoms. Therefore, tungsten oxide has many non-stoichiometric compounds, such as $WO_{2.72}$, $WO_{2.8}$, $WO_{2.83}$ and $WO_{2.9}$. Of these, $WO_3$ is the most common and has been widely studied as a typical photocatalytic water oxidation semiconductor material. $WO_3$ is a typical narrow-band gap indirect semiconductor with a forbidden band width of 2.6–2.8 eV, which can absorb part of the visible light [64]. In addition, $WO_3$ is a research hotspot in the field of photoelectrochemical water splitting because of its high carrier mobility, stability in acidic electrolytes and resistance to photocorrosion.

#### 3.2.1. Morphology Control

$Bi_2WO_6$ is one of the tungsten-based materials that belongs to Aurivillius crystal oxides. Its crystal has an orthorhombic system, and its narrow band gap (2.7–2.9 eV) structure allows it to meet the response absorption of visible light. Moreover, its stable structure and eco-friendly properties have attracted many scientific researchers to study it. Since the valence band of $Bi_2WO_6$ is composed of $O_{2p}$ and $Bi_{6p}$, and the conduction band is composed of $W_{5d}$-assisted Bi6p orbitals, the VB energy levels can be dispersed broadly. By employing the Kirkendall effect in ion exchange and BiOBr precursor, Huang et al. [65] prepared a bowl-shaped $Bi_2WO_6$ HMS material. Based on the large specific surface area of the material, its adsorption capacity for $CO_2$ reaches 12.7 mg $g^{-1}$ at room temperature and pressure. The material adsorbs a large number of $HCO_3^-$ and $CO_3^{2-}$ species on the surface during the reaction, which makes the catalytic reaction easier. The $Bi_2WO_6$ HMS thus has a high catalytic activity, and the methanol yield is 25 times higher than that of the $Bi_2WO_6$ SSR.

Iron phthalocyanine FePc is neatly assembled on porous $WO_3$ under induction and coupled with surface atoms by H-bonding [66]. The optimized FePc/porous $WO_3$ nanocomposites exhibit enhanced $CO_2$ photoreduction activity, which is attributed to the synergistic effects of a high specific surface area, a better charge separation and proper central metal cation. A series of mesoporous $WO_3$ with interconnected networks were synthesized by the silica KIT-6 hard template method [67], which became oxygen-deficient after hydrogenation treatment. Both the ordered porous structure and oxygen vacancies contributed to the increased yield of $CH_4$ and $CH_3OH$.

$WO_3$ with a hollow nest morphology with hierarchical micro/nanostructures (HNWMs) was synthesized [68] by the one-step hydrothermal method (Figure 10), with a particle diameter of about 2.5 μm. The 2D nanosheets, which have an average thickness of 30–40 nm, were assembled to build a distinctive hollow nest structure with a good stability and reusability under visible light. Hao et al. [69] prepared core–shell heterojunctions of two-dimensional lamellar $WO_3/CuWO_4$ by the in situ method. After the modification of amorphous Co-Pi co-catalyst, the photoanode of ternary homogeneous core–shell structure exhibited a high photocurrent of 1.4 mA/$cm^2$ at 1.23 V/RHE, which was 6.67 and 1.75 times higher than that of the pristine $WO_3$ and 2D homogeneous heterojunction. Ren et al. [70] synthesized unique flower-like $Bi_2WO_6$/BiOBr catalysts by the simple one-step solvothermal method, and showed that the photocatalytic activity of the composites was significantly enhanced due to the construction of type II heterojunctions. The presence of Br source enhanced the light absorption and improved charge-carrying spatial transfer and separation.

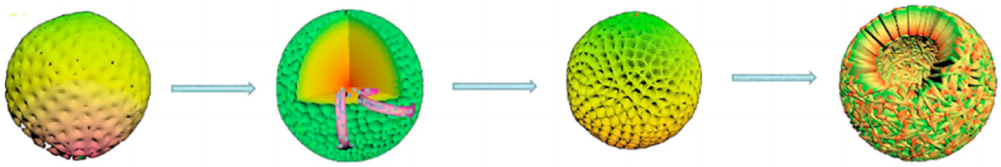

**Figure 10.** Schematic diagram of the HNWM formation process [68].

Ti atoms in ultrathin Ti-doped $WO_3$ nanosheets promoted the charge transfer [71], as they accelerate the generation of key intermediates COOH*, which was revealed by in situ characterization. Furthermore, Gibbs free energy calculations were calculated to verify that ion doping can reduce the $CO_2$ activation energy barrier and $CH_3OH$ desorption energy barrier by 0.22 eV and 0.42 eV, respectively, thus promoting the formation of $CH_3OH$. The ultrathin Ti-$WO_3$ nanosheets showed an excellent $CH_3OH$ yield of 16.8 μmol $g^{-1}$ $h^{-1}$. Two-dimensional bilayered $WO_3$@$CoWO_4$ were prepared [72] via a facile interface-induced synthesis method. The optical energy conversion efficiency can be improved by both p–n heterojunctions and interfacial oxygen vacancies. The narrow band gap of the $WO_3$@$CoWO_4$ heterojunction was proved by DFT calculations and some characterizations, which allows a better visible light absorption. A tree-like $WO_3$ film was prepared [73] by the hydrothermal process, which has a large specific surface area. The $WO_3$ product was a unity of hexagonal/monoclinic crystals, which contained $W^{5+}$ defects and oxygen vacancies. The products were further subjected to a mild reduction solution at the lower temperature of 333 K to introduce more defects. It turns out that the intermediate state induced by defects diminished the band gap. A reasonable amount of defects benefits the photocatalytic activity of $WO_3$, while too many defects impair its catalytic capacity. The performance of the treated $WO_3$ films increased 2.1 times in 48 h compared to that of the annealed $WO_3$ samples.

Preferentially Exposed Facets

According to studies, infrared (IR) light makes up nearly 50% of solar energy, and it is challenging to make use of the majority of the light. Liang et al. [74] fabricated 2D ultrathin $WO_3$ with an intermediate band gap. They achieved the first complete decomposition of $CO_2$ driven by infrared light without the addition of sacrificial agents. Theoretical calculations indicated that the generation of the intermediate energy band resulted from the critical density of the generated oxygen vacancies, which has also been verified by synchrotron valence band spectroscopy, photoluminescence spectroscopy, ultraviolet-visible-near-infrared spectroscopy and synchrotron infrared reflection spectroscopy. The results showed that the $WO_3$ atomic layer containing oxygen vacancies can achieve the complete decomposition of $CO_2$ and generate CO and $O_2$ under infrared light.

Microscopic $WO_3$ nanocrystals were formed by Chen et al. [75] through solid–liquid phase arc discharge in an aqueous solution. Then, they synthesized ultrathin single-crystal $WO_3$ nanosheets via a laterally oriented attachment method. The quantization effect of this nanostructure altered the bandgap width of $WO_3$ nanosheets, enabling the semiconductor to exhibit a high performance at a wide range of nanometer sizes. It is beneficial to control the activity and selectivity of the photoconverted $CO_2$ products. As a consequence, $WO_3$ with a strong visible light response has enormous potential in the field of photocatalytic $CO_2$ reduction.

$Bi_2WO_6$ has a positive conduction band potential, which is not enough to excite and reduce $CO_2$ molecules, thus limiting its application in the photocatalytic reduction of $CO_2$. Therefore, researchers have been devoted to modifying the surface of $Bi_2WO_6$ to improve its photocatalytic activity in order to obtain a high-efficiency $CO_2$ reduction ability. Zhou et al. [76] successfully prepared $Bi_2WO_6$ nanosheets with a monolayered structure by introducing the surfactant CTAB (hexadecyltrimethylammonium bromide) into the precursor solution. A large number of unsaturated Bi atoms were produced, which provided sufficient active sites for photocatalytic reactions. $Bi_2WO_6$ is composed of a

$[BiO]^+$-$[WO4]^{2-}$-$[BiO]^+$ sandwiched layer structure. Under irradiation, holes and electrons are generated in different $[BiO]^+$ layers. This structure promotes the spatial separation of photogenerated electron–holes and greatly reduces the carrier recombination rate of the monolayer $Bi_2WO_6$ material.

With the assistance of an oil-based primary amine ($C_{18}H_{37}N$) surfactant, Zhou et al. [77] conducted a hydrothermal reaction at 200 °C for 20 h to prepare an ultra-thin and uniform $Bi_2WO_6$ nanosheet. The material has a strong response under visible light, and its forbidden band width was about 2.44 eV through theoretical calculations, with a conduction band potential of −0.31 e V. Then, $CO_2$ could be easily reduced to $CH_4$, and its yield was 20 times higher than that of SSR $Bi_2WO_6$. The light-absorbing capacity will decrease if the nanosheets are too thin because of the quantum size effect. Therefore, scholars need to consider roundly when designing fresh material [78].

DOM Structure W-Based Materials

Unexpectedly, it was found that the resistance of 3DOM-$WO_3$(270) and the $Ag_3PO_4$ electron absorption band were comparable. By depositing $Ag_3PO_4$ nanoparticles in the micropores of 3DOM-$WO_3$, Chang et al. [79] achieved a higher photocatalytic activity and more efficient light harvesting at the wavelengths of 460–550 nm. A Z-scheme g-$C_3N_4$/3DOM-$WO_3$ catalyst designed by Tang et al. [80] also has a high $CO_2$ photoreduction activity. The separation way of the photogenerated electron–hole pairs determined its Z structure, and 3DOM framework heightened the light collecting efficiency. Therefore, an excellent photocatalyst exhibited a high CO evolution rate of 48.7 μmol $g^{-1}$ $h^{-1}$.

3.2.2. Heterojunction

Quantum dot composite: CuO quantum dots (QDs) were combined with $WO_3$ nanosheets by a self-assembly method and the diameter of 6%CuO QDs/$WO_3$ NSs was mainly located at 1.6 nm [81]. The bandgap energy of CuO/$WO_3$ fell in 2.28 eV and the complex catalyst possessed a lower resistance for charge carrier transfer that showed in UV-vis DRS and EIS analysis. Due to the low CB position, CO cannot be obtained when using pure $WO_3$. However, the photogenerated electrons gathered in the $WO_3$ CB position was able to reach the CuO VB position when the Z-scheme (Figure 11) was formed by intimate heterojunctions. At the same time, the reduction reaction that transformed $CO_2$ into CO occurred at the CuO CB position. The high yield rate of about 1.58 mmol $g^{-1}$ $h^{-1}$ also benefited from a longer fluorescence lifetime, and reduced the overlap of electron pore pairs.

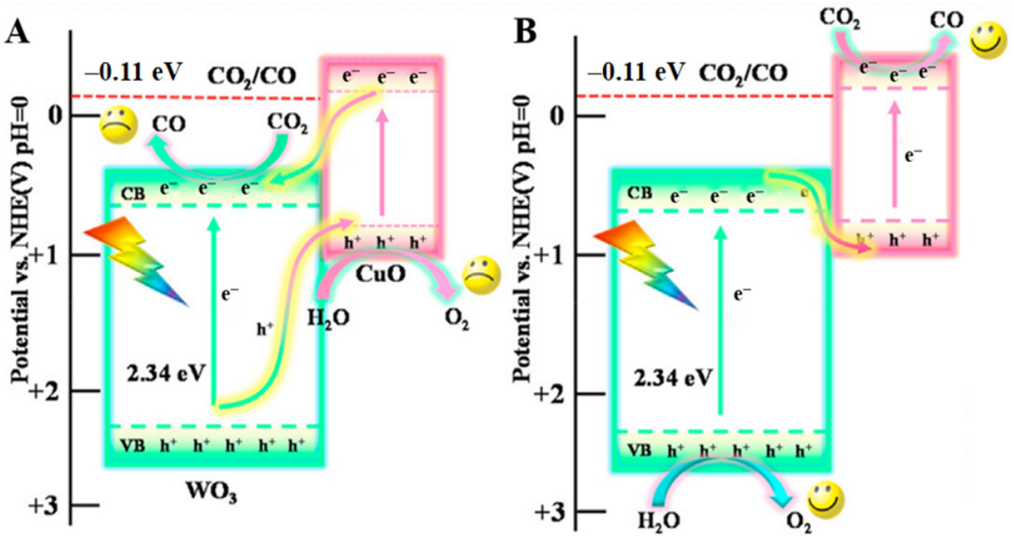


**Figure 11.** The proposed charge transfer mechanisms: (**A**) II-scheme and (**B**) Z-scheme for CuO/$WO_3$ [81].

Perovskite composite: For $WO_3$, the negative potential energy of the sheet shape (−31.5 mV) was lower than that of the rod (−21.0 mV). In addition to its potential advantages, S–$WO_3$ offers a higher specific surface area. Defects occurred because of the exposed interior atoms in nanosheets surface, which promoted the $CO_2$ adsorption. Positively charged perovskite cesium lead tribromide ($CsPbBr_3$, CPB) with a long electrically diffused length was selected to be combined with S–$WO_3$, affording a high field rate of CO and $CH_4$. Zhang and others [82] employed a three-dimensional hydrophobic porous melamine foam to support the mixture, not only to protect the CPB from dissolution but also to reduce toxic $Pb^{2+}$.

#### 3.2.3. Ion Doping

Molybdenum with a similar ionic size was chosen to dope the $WO_3$ as a low-valence metal species. The $W^{5+}/W^{6+}$ ratio of the catalyst was increased, making it easier to exchange electrons with reactants. The conductivity of protons was enhanced by the presence of hydrogen bronze, which originated from a chemical reaction between $WO_3$ and Brønsted protons and excess electrons in their lattices. Wang et al. [83] prepared molybdenum-doped $WO_3 \cdot 0.33\ H_2O$ by the hydrothermal method. The $E_{cb}$ and $E_{vb}$ energy were both higher at 3%Mo-WO than $WO_3$. After 20 min of the FTIR spectra, rare intermediate $CO^{2-}$ was observed, verifying the activation of $CO_2$, which was more common in low-valent meta species. The content of potassium hydroxide in an aqueous solution obtained by photocatalytic water oxidation was higher and the $CH_4$ yield was 4.2 times higher than $WO_3$.

#### 3.2.4. Summary

To date, $Bi_2WO_6$ semiconductor photocatalytic materials have made great progress in the field of environmental management. Some photocatalytic systems using $WO_3$-based materials in $CO_2$ conversion are listed in Table 2.

**Table 2.** Summary of the recent results on the photoreduction of $CO_2$ by $WO_3$-based materials.

| Type of Enhancement | Photocatalyst | Description | Conditions (Lamp, Cutoff Filter) | Product Yield/ $\mu mol \cdot g^{-1} \cdot h^{-1}$ | Refs. |
|---|---|---|---|---|---|
| Heterojunction | Pd-Au/$TiO_2$–$WO_3$ | 0.5%Pd−0.1 wt%Au | 400W Hg | CO 225.5<br>$CH_4$ 15.1 | [84] |
| | $Bi_2WO_6$/Si | $Bi_2WO_6$: Si = 1:1 | 300 W Xe<br>420 nm | $C_2H_5OH$ 201 | [85] |
| S-scheme | CdS/$WO_3$ | CdS nanoparticles at the $WO_3$ surface | 300 W Xe<br>420 nm | CO 35.625<br>$CH_4$ 3.75 | [86] |
| | $WO_3$/$CsPbBr_3$ | 3D porous melamine foam-supported | 300 W Xe | CO+$CH_4$ 600 | [82] |
| Z-scheme | $WO_3$-$TiO_2$/$Cu_2ZnSnS_4$ | Mesoporous ternary heterostructure | 400 W Xe420 nm | CO 15.37<br>$CH_4$ 1.69 | [87] |
| | $WO_3$/g-$C_3N_4$ | 3D/2D hollow microspheres | 35 W HID car lamp and 300 W Xe ($H_2$ reduction) | CO 145<br>$CH_4$ 133 | [88] |
| | $TiO_2$/$WO_3$/Pt | 1D continuous fibrous structure | 300W Xe | $H_2$ 128.66 | [89] |
| | CuO Dots/$WO_3$ | CuO quantum Dots/$WO_3$ nanosheets | 300 W Xe400 nm | CO 1.58 | [81] |
| Ion doping | 3%Mo-WO | Mo-doped $WO_3 \cdot 0.33H_2O$ nanorods | 500 W Xe | $CH_4$ 5.3 | [83] |
| 3DOM | g-$C_3N_4$/3DOM-$WO_3$ | 300 W Xe<br>420 nm | visible light (≥420 nm) | CO 48.7<br>$CH_4$ 7.5 | [80] |

### *3.3. ZnO-Based Photocatalysts*

ZnO, a common metal oxide, is a n-type semiconductor with an *Eg* value of 3.37 eV. It is a kind of amphoteric oxide that has the advantages of nontoxic harmlessness, low cost, abundant reserves, convenient preparation, low dielectric constant and low optical coupling rate. ZnO has three main lattice structures: wurtzite structure, zinc-blended structure and tetragonal rock salt structure. The wurtzite structure is considered the most stable and common structure in nature. It is a kind of hexagonal crystal, in which the O and Zn atoms are aligned with the hexagonal density stacking. The photodegradation process of ZnO is similar to $TiO_2$ and it has been widely used in photocatalysts, solar cells and conducting materials.

#### 3.3.1. Morphology Control

The 3nm Pt particles were uniformly dispersed over ZnS@ZnO with a mesoporous heterostructure [90] and more $CH_3OH$ was obtained. Reactant charge carriers entered the pore channels of the porous heterozygous layer, thus reducing the likelihood of flow resistance and electron–hole recombination. The S-scheme photocatalyst delivered a high $CH_3OH$ formation rate of 81.1 μmol $g^{-1}$ $h^{-1}$, which is roughly 40 and 20 times larger than that of bare ZnO (3.72 μmol $g^{-1}$ $h^{-1}$) and ZnO–ZnS (4.15 μmol $g^{-1}$ $h^{-1}$). On the other hand, a porous ZnO@ZnSe core/shell nanosheet array material (Figure 12A) was prepared in a controlled manner [91]. The final n-type semiconductor composites had a proper negative CB band edge. In comparison to ZnO or ZnSe, more pairs of electron–holes were formed under visible light. Electrons tend to land on ZnO, which is aimed at methanol production. Mei et al. prepared a ZnO microsphere with different numbers of shells [92] and the photoelectric performance of ZnO was optimal when the number of shells reached three.

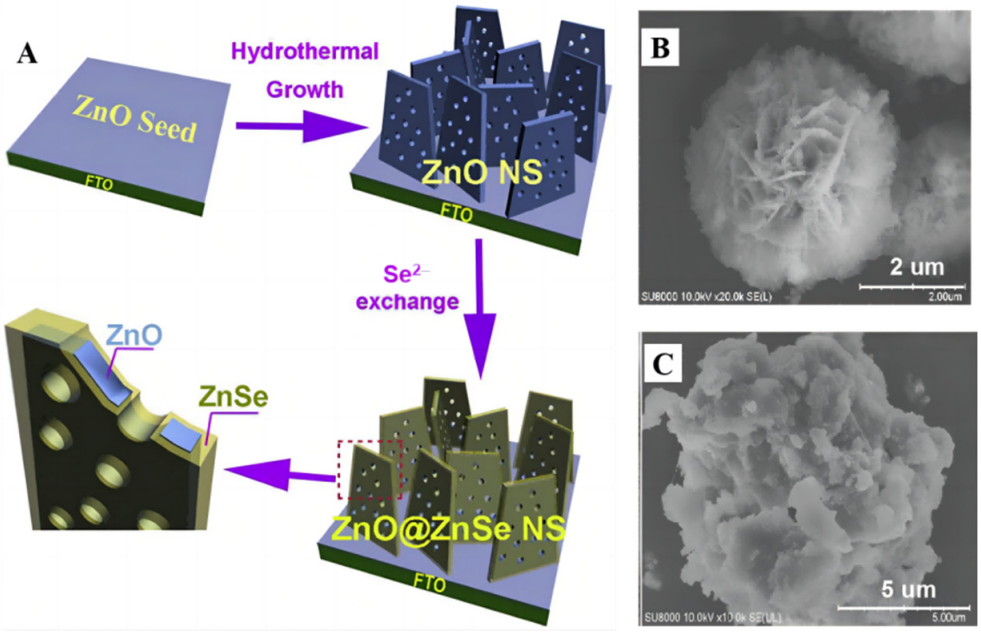


**Figure 12.** (**A**) Schematic illustration of the fabrication process of ZnO@ZnSe photocathode [88]. (**B**) ZnO/ZnS (**C**) ZnO/ZnS/g-$C_3N_4$ SEM images [91].

It is challenging to coat uniform 2D g-$C_3N_4$ nanofilm on the surface of 3D materials because of the difficulty in exfoliation process. Thus, Wang et al. [93] proposed an electrostatic method and incorporated g-$C_3N_4$ nanofilm with porous ZnO nanospheres that has a strong interaction. The heterojunction was then anchored on 3D graphene aerogels (GAs). The compound g-$C_3N_4$/ZnO/GA has extraordinary stability, maintaining a high $CO_2$ conversion rate, which is 92% of its original activity after 100 h.

ZnO/ZnS nanoflowers (Figure 12B) were combined with g-$C_3N_4$ nanosheets (Figure 12C) to construct a double Z-scheme structure [94]. ZnO/ZnS nanoflowers provide a large specific surface area and g-$C_3N_4$ helps to absorb more photons under solar light irradiation. Optimized interfacial charge transfer dynamics in ternary heterostructure can be characterized by photocurrent measurements. As a result, the formation rate of $H_2$ product over the novel double Z-scheme mixture increases to 301 μmol $g^{-1}$ $h^{-1}$ on water splitting.

Hierarchical CuO/ZnO nanocomposites with p-n heterojunction were prepared [95] by the modified hydrothermal method. The photocatalysts are found to converse $CO_2$ to methanol in aqueous solution containing dimethylformamide (DMF) and triethylamine (TEA) as electron donor under visible light irradiation. ZnO/NiO porous hollow spheres with sheet-like subunits were obtained [96] by calcination of Ni-Zn MOFs. Numerous p-n heterojunctions with n-type ZnO and p-type nickel monoxide were formulated in mixed ZnO/NiO. The porous hollow structure with the large specific surface area can increase the absorption capacity of $CO_2$ and light.

Based on the vapor to solid mechanism, a novel ternary Ag/$CeO_2$/ZnO nanocomposite [97] was synthesized by the facile thermal decomposition method. Oxygen vacancies introduced by line structure contributied to a narrow band gap of 2.66 eV, and this was further confirmed by DRS characterization. After the preparation of the ZnO/$TiO_2$ nano-tree arrays, $Ag_2S$ and ZnS were synthesized to modify the nano-tree arrays by cation exchange methods [98]. The core-shell structure of ZnO@ZnS prevented the decomposition of ZnO, and the modification of $Ag_2S$ reduced the *Eg* value of the composite and promoted the red-shifted of light absorption.

#### 3.3.2. 3DOM Structure Zn-Based Materials

Wang et al. [99] published metal-organic-framework-derived 3DOM N-C doped ZnO (Figure 13) for efficient $CO_2$ reduction. The ultra-tiny $CoO_x$ clusters were anchored on the surface of catalyst and no Co-Co peak was found in $CoO_x$/N-C-ZnO. The charge transfer rate was jacked up by ion doping and the recombination of electron-hole pairs was tamed because of the $CoO_x$ clusters. Furthermore, $CoO_x$ on the orderly connected channels can act as an electron trap to capture electrons, which makes a contribution to photoreaction efficiency. The density theory calculations (DFT) was also used to detect the $CO_2$ adsorption ability, and $CoO_x$/N-C-ZnO exhibited the most negative $CO_2$ binding energy due to improved electron structure of adsorption site.

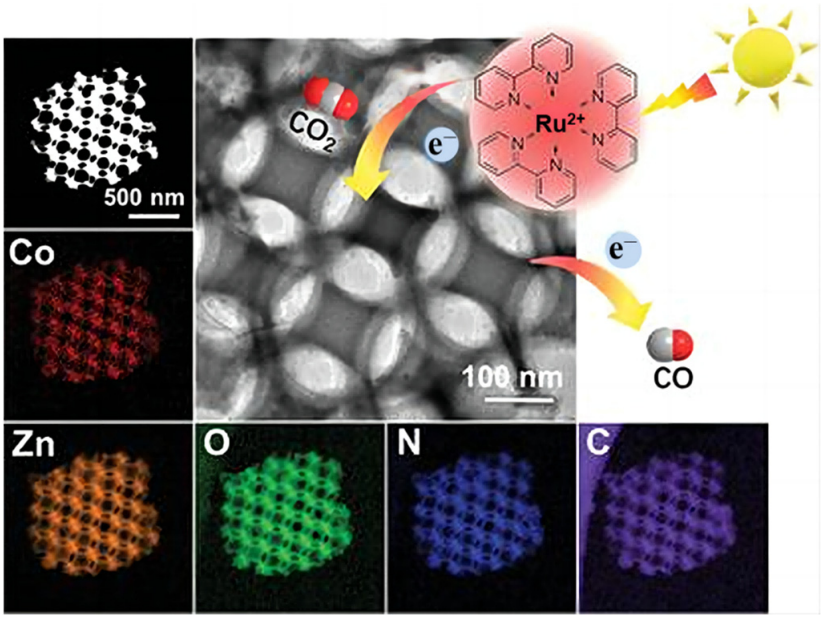


**Figure 13.** HAADF-STEM image of $CoO_x$/N-C-ZnO and related elemental mapping images [99].

### 3.3.3. Heterojunction

Recently, zeolitic framework (ZF) composite fabricated by the microwave-hydrothermal synthesis method (MWH) has attracted attention, which can provide a fast heating-speed and produce morphologically uniform samples. With biodegradable template, the zeolitic framework (ZF) was synthesized via MWH method from volcanic ashes. The $NaAlSiO_4$ (NAS) framework was composed of 50 nm circular channels and has a large surface area. Hip'olito et al. [18] embedded ZnO/CuO hybrid structure in the NAS channels, resulting in a ternary composite. The synergistic effect among ZnO, CuO and ZF support accelerated the photocatalytic process of water splitting and $CO_2$ reduction, which offers higher $H_2$ and HCOOH evolution rate.

The imidazole framework-8 (ZIF-8) molecular as a widely used zeolite (ZIF) composite, has an excellent competence of absorbing $CO_2$, which is apt for $CO_2$ converting. Selective-breathing effect was wielded to boost $CO_2$ conversion efficiency through monolithic NF@ZnO/Au@ZIF-8 (Figure 14A) catalyst [100]. Au particles were loaded on ZnO nanorods that grown on Ni foam (NF), the mixture was immersed in methylimidazole solution (Figure 14B). Based on the results of electrochemical impedance spectroscopy (EIS) Nyquist plots, the alternating magnetic field was introduced to create magnetic heat, which leading to increased carrier density and improved photocatalytic performance. It is found that the selectivity of $CH_4$ cheeringly achieved 89% from 61% under photo-thermal-magnetic coupling effect.

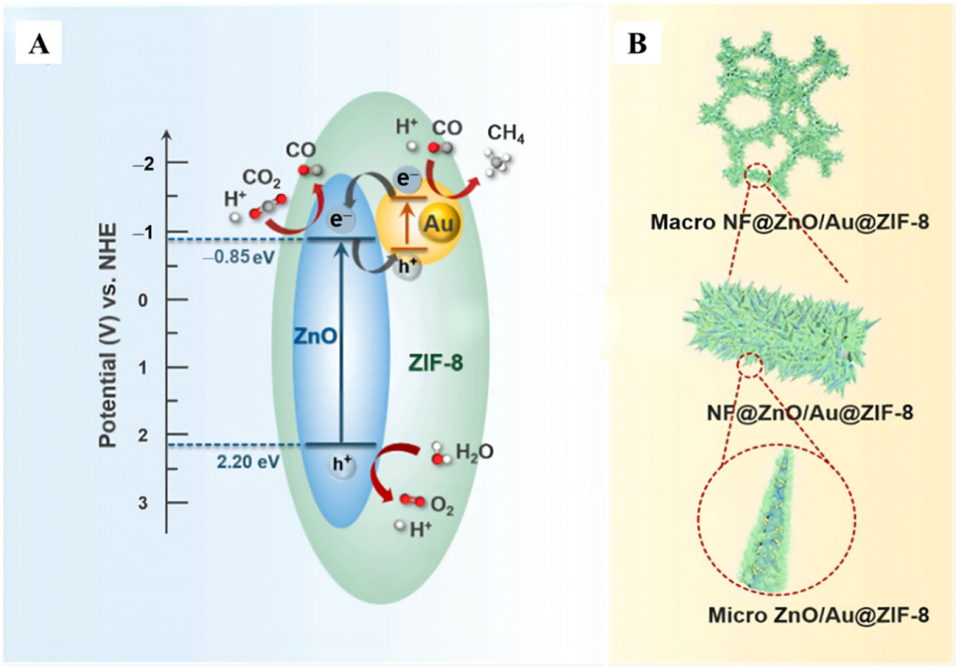


**Figure 14.** (**A**) Illustration of the band structure and charge transfer process of NF@ZnO/Au@ZIF-8 catalyst under UV− vis light. (**B**) The structural diagram the monolithic NF@ZnO/Au@ZIF-8 photocatalyst [100].

### 3.3.4. Ion Doping

Many metal elements have been doped in ZnO to minish its band gap, such as Sb, Cu and Mn, among them Co distinguished itself because of the similar ion radius. In addition, the conversion of $Co^{3+}$ and $Co^{2+}$ results in oxygen vacancies, which greatly enhances photocatalytic efficiency. Xie et al. [101] introduced $Co^{3+}$ with different mole ratio to ZnO microspheres precursor (including $Zn^{2+}$, urea, and PVP), and the introduction of $Co^{3+}$ did not disrupt lattice structure as seen in the XRD model. It was revealed that the presence of both $Co^{2+}$ and $Co^{3+}$ in Co-ZnO from high-resolution spectrum, and $Zn_{2p}$ exhibited higher binding energy due to $Zn^{2+}$ charge transfer in 7% Co-ZnO. As the ratio

of Co/Zn increased, the conversion from $Co^{2+}$ to $Co^{3+}$ decreased, and the light response range gradually expanded. The results showed that the electrochemical impedance of 7% Co-ZnO sample was the lowest band gap of 2.56 eV.

#### 3.3.5. Summary

Great efforts have been made to design catalysts for $CO_2$ reduction on ZnO and the relevant research data are summarized in Table 3.

**Table 3.** Summary of the recent results on the photoreduction of $CO_2$ by $WO_3$-based materials.

| Type of Enhancement | Photocatalyst | Description | Conditions (Lamp, Cutoff Filter) | Product Yield/ $\mu mol \cdot g^{-1} \cdot h^{-1}$ | Refs. |
|---|---|---|---|---|---|
| Heterojunction | Cu-ZnO Cel-T | Cellulose template designed porous ZnO | 300 W Xe | CO 30.17 | [102] |
| | OD-ZnO/C | Carbon dots, spherical morphology | 400 W Xe | CO 118.8(600 °C) | [103] |
| | Pt/ZnO–ZnS | Porous ZnS–ZnO | 300 W Xe, 420 nm | $CH_3OH$ 81.8 | [90] |
| Z-scheme | Ag-$Cu_2O$/ZnO | 0.6Ag−0.4$Cu_2O$ ZnO nanorods | 300 W Xe | CO 3.36 | [104] |
| | g-$C_3N_4$/ZnO/graphene aerogel | Porous ZnO nanosphere | 300 W Xe, 420 nm | CO 33.87 | [93] |
| | ZnO/ZnS/g-$C_3N_4$ | Spherical ZnS, ZnO nanoflowers | 300 W | $H_2$ 301 | [94] |
| p–n hetero-junction | ZnO/CuO/Zeolite | ZnO/CuO in $NaAlSiO_4$ channels | two 20 W halogen lamps | $H_2$ 62.3 HCOOH 907 | [18] |
| Ternary catalyst | R-ZnO@ LDH | Core–shell Structure, belt-like ZnO hierarchical LDH | 300 W Xe | $CH_4$ 11.4 | [105] |
| 3DOM | $CoO_x$/N-C-ZnO | N, C doped | 420 nm | CO 26.4 | [99] |

### *3.4. $Cu_2O$-Based Photocatalysts*

Cuprous oxide ($Cu_2O$) is a potential p-type semiconductor with a wide visible-light response range and high photo-electric conversion efficiency (18%) [106], and it displays attractive prospects in solar energy conversion and heterogeneous photocatalysis. Although $Cu_2O$ possesses many excellent properties, photocorrosion and the rapid recombination of $e^-/h^+$ pairs affect its activity and limit its application. The photocorrosion is believed to occur in two ways: (1) self-reduction caused by generated electrons and (2) self-oxidation caused by the generated holes.

$$\text{Self-reducing photocorrosion: } Cu_2O + H_2O + 2e^- \rightarrow 2Cu + 2OH^- \quad (10)$$

$$\text{Self-oxidative photocorrosion: } Cu_2O + 2OH^- + 2h^+ \rightarrow 2CuO + H_2O \quad (11)$$

Therefore, developing Cu-based catalysts with excellent activity, selectivity and stability has become the research hotspot in the area of the photocatalytic reduction of $CO_2$. Many successful attempts have been made to improve the photostability and photocatalytic performance of $Cu_2O$. In general, most studies focus on enhancing the charge transfer from $Cu_2O$ to reactants or cocatalysts to prevent charges from accumulating within the particles. A series of methods for improving the performance of $Cu_2O$ are discussed in detail in what follows.

#### 3.4.1. Morphology Control

A branch-like $Cd_xZn_{1-x}Se$ nanostructure was obtained [107] by the cation-exchange method, which was then mixed with $Cu_2O$@Cu to form heterojunctions. Selenium (Se) vacancies were created during the ion exchange process and the crystal growth was lim-

ited due to the additive diethylenetriamine (DETA), leading to insufficient coordination of the surface atoms, which then become active adsorption sites. Highly hierarchical branching-like structures assembled by one-dimensional structural materials not only facilitate electron accumulation at their tips but also increase the light-accepting area, and characterization results show that branching structures can effectively absorb visible light. $Cd_{0.7}Zn_{0.3}Se/Cu_2O$@Cu step-scheme heterojunction exhibited a CO release yield of 50.5 μmol $g^{-1}$ $h^{-1}$.

Ultrafine cuprous oxide U-$Cu_2O$ (<3 nm) was grown on the polymeric carbon nitride (PCN) (Figure 15) by the in situ method [108]. PCN has a narrow band gap of 2.7 eV that can capture visible light. Both ultrafine nanoclusters and Z-scheme heterojunction can protect U-$Cu_2O$ from degradation. The photocatalyst U-$Cu_2O$-LTH@PCN has high stability, maintaining more than 95% activity after five cycles of testing, while bare $Cu_2O$ grades completely within three cycles. A large number of heterojunctions were formed by U-$Cu_2O$ particles and lamellar PCN, expediting the electron transfer efficiency. The product can convert $CO_2$ to methanol with water vapor under light irradiation at the high yield of 73.46 μmol $g^{-1}$ $h^{-1}$. Ultrathin $Ti_3C_2$MXene with a high fraction of coordinated unsaturated surface sites was fabricated by Zhang et al. [109]. Via the HF etching method, different amounts of $Cu_2O$ were combined with $Ti_3C_2$ nanosheets under the hydrothermal condition. The unique hexagram morphology of $Cu_2O$, the 2D layer structure and excellent conductivity of $Ti_3C_2T_x$ nanosheets and the synergistic effect between the two composites promote the improvement of photoactivity. Zhang et al. reported the bifunctional catalyst of $Cu_2O$@$Fe_2O_3$. $Cu_2O$ nanoparticles coated with an $Fe_2O_3$@carbon cloth electrode were used for both overall water splitting and $CO_2$ photoreduction [110].

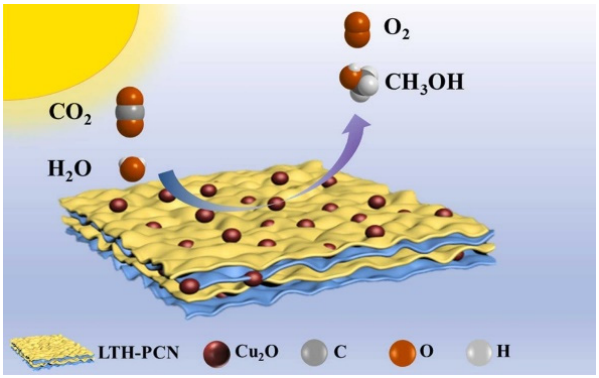


**Figure 15.** Ultrafine U-$Cu_2O$ nanoclusters anchored on the photosensitizing PCN support [108].

Preferentially Exposed Facets

$Cu_2O$ is an ideal compound to study the influence of electron-related effects. The rare occurrence of the O-Cu-O 180° linear coordination of $Cu_2O$ makes its (111), (100) and (110) facets chemically active. Zhang et al. [111] successfully achieved the morphology control of $Cu_2O$ nanocrystals by utilizing the selective surface stabilization of PVP on the (111) plane of $Cu_2O$. With different amounts of PVP, the surface area ratio of (111) to (100) was subtly tuned, which resulted in the shape evolution of the system and various $Cu_2O$ structures (Figure 16). The detailed modification mechanism was elucidated from the structural and kinetic perspectives.

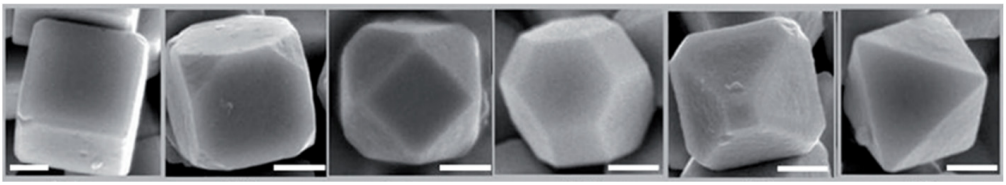

**Figure 16.** FESEM images of the $Cu_2O$ polyhedrons with different volume ratios of (100) to (111) [111].

Octahedral copper oxide that exposes the (111) crystal faces was decorated with low Fermi energy Ag nanoparticles. After coating with rGO, the ternary heterojunction catalyst [112] exhibits selective photocatalytic superiority towards $CH_4$. The CO* radicals can be characterized via DRIFT spectra and DFT calculations, which is the key intermediate for the conversion of $CO_2$ to $CH_4$. Two types of $MoS_2$ (p-type and n-type) and two shapes of $Cu_2O$ (cubic and octahedron) were synthesized and combined with each other [113], and the compositions possessed different electronic and structural properties. The heterostructures formed by the p-type $MoS_2$ with intrinsic conductivity had a higher photocatalytic activity, and the methanol production yield was as high as 76 μmol $g^{-1}$ $h^{-1}$. Both Z-type and ii-type charge transfer mechanisms were built using an n-type $MoS_2$ mixture. For $Cu_2O$, the cubes of the exposed (100) crystal plane with a higher binding affinity with $MoS_2$ transferred electrons more efficiently and produced methanol at a higher rate.

A 3D porous Cu was produced by electrodeposition method [114], being transformed into $CuO_2$ after following high-temperature annealing. Three-dimensional $Cu_2O$ delivers a 24-fold production of CO compared with the unremarkable and non-porous Cu. Additionally, more $CO_2$ accumulated and took reactions in the hollow space of 3D $Cu_2O$ to form $C_2$ products.

3DOM Structure Cu-Based Materials

The 3DOM $Cu_2O$ structure was luckily obtained [115] via polystyrene crystal templates. Under the contrived "sunlight" irradiation, incident light was reflected and absorbed around and around again. In the ultra-visible absorption spectra (350 to 800 nm), $Cu_2O$ with large orifices absorbs more photons than bulk samples, making it more advisable for solar applications. 3DOM $Cu_2O$ was prepared [116] by the electrochemical method to reduce $CO_2$, and its Faraday efficiency was five times higher than that of Cu film. The $CO_2 \cdot^-$ intermediate in 3DOM channels is more stable and leads to the possibility of forming CO and HCOOH products (Figure 17). We look forward to the applications of inverse opal $Cu_2O$ in photocatalysis.

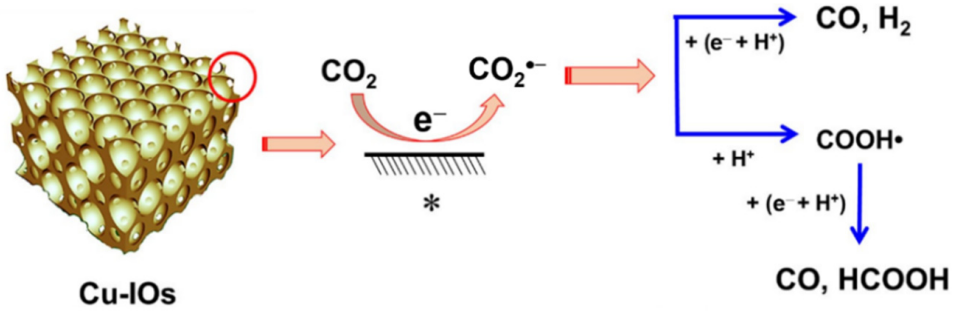


**Figure 17.** Proposed mechanism for $CO_2$ reduction to CO and HCOOH on $Cu_2O$-derived Cu-IOs (The symbol "*" represents the surface.) [116].

3.4.2. Heterojunction

Liu et al. [117] reported a facile solution and chemistry route to synthesize rGO-incorporated crystal $Cu_2O$ with various facets as visible-light-active photocatalysts for $CO_2$ reduction. The enhanced activity was attributed to the formation of the heterojunction and the existence of rGO as the electron transport mediator. M. Flores et al. [118] adopted the microwave-hydrothermal method to couple the powders of $Mg(OH)_2$, CuO and $Cu_2O$. The synthesis method allowed a sufficient interaction between $Mg(OH)_2$/CuO and $Cu_2O$ without inhibiting the gas adsorption capacity of $Mg(OH)_2$. They found that the presence of $Cu_2O$ favored the selectivity towards $CH_3OH$ production because a higher $Cu^+$ concentration led to better selectivity. Niwesh et al. [119] reported the formation of a p–n heterojunction between $Cu_2O$ and the $SnS_2/SnO_2$ nanocomposite that offered favorable reductive potentials and high stability, mainly owing to their intimate interfacial contact. In the absence of a sacrificial agent, the generation rate of $NH_4^+$ was

66.35 μmol $g^{-1}$ $h^{-1}$ for $Cu_2O/SnS_2/SnO_2$, which is 1.9-fold higher than that of $SnS_2/SnO_2$. However, the work of Trang et al. also demonstrated the instability and photo-oxidation of $Cu_2O$ heterojunctions. Generally, most p–n heterojunctions are found to reduce the redox capacity of photogenerated charges. This is especially evident for $Cu_2O$ p–n type heterojunctions, as CuO is excessively formed on the surface of $Cu_2O$ under continued illumination, so there are recombination problems at the heterojunction interface. The construction of Z-scheme heterojunctions overcomes the limitations of p–n heterojunctions, namely the reduction in redox potential and charged carrier recombination at the p–n heterojunction interface. In a Z-type heterojunction, the redox potential can be maintained under the premise of high photo-induced electron transport rate.

Zhang et al. [120] synthesized coal-based CNPs with an $sp^2$ carbon and multilayer graphene lattice structure, and loaded them onto the surface of $Cu_2O$ nanoparticles prepared by the in situ reduction of copper chloride. The rapid recombination of electron–hole pairs was suppressed by the introduction of CNPs. The energy gradient formed on the surface of $Cu_2O$/CNPs facilitates the effective separation of electron–hole pairs for $CO_2$ reduction, improving the photocatalytic activity. Atomically dispersed In-Cu bimetallic catalysts were prepared [121] by the in situ pyrolysis method, in which carbon nitride acted as a carrier. The light-harvesting and charge separation efficiency were enhanced by regulating the loading amount of Cu and In, and the supreme generation rate of the photoreduction of $CO_2$ to ethanol reached 28.5 μmol $g^{-1}$ $h^{-1}$ with 92% selectivity. The DFT calculations showed that the introduction of an In atom in copper can accelerate electron transfer from carbon nitride to metal, improve the charge separation efficiency and increase the electron density of copper active sites. The presence of In–Cu sites exerted a synergistic effect, which could promote C–C coupling, lower the energy barrier of *COCO generation and increase ethanol yield. Zhao et al. [122] reported the indirect Z-scheme heterojunction of UiO-66-$NH_2$/$Cu_2O$/Cu, which achieved a high $CO_2$ photocatalytic conversion to CO. The SEM results of $Cu_2O$, UiO-66-$NH_2$ and U/C/Cu-0.39 are shown in Figure 18A–C. In this catalytic system, UiO-66-$NH_2$ slowed down the photo-corrosion rate of $Cu_2O$ and increased the $CO_2$ adsorption capacity (Figure 18D).

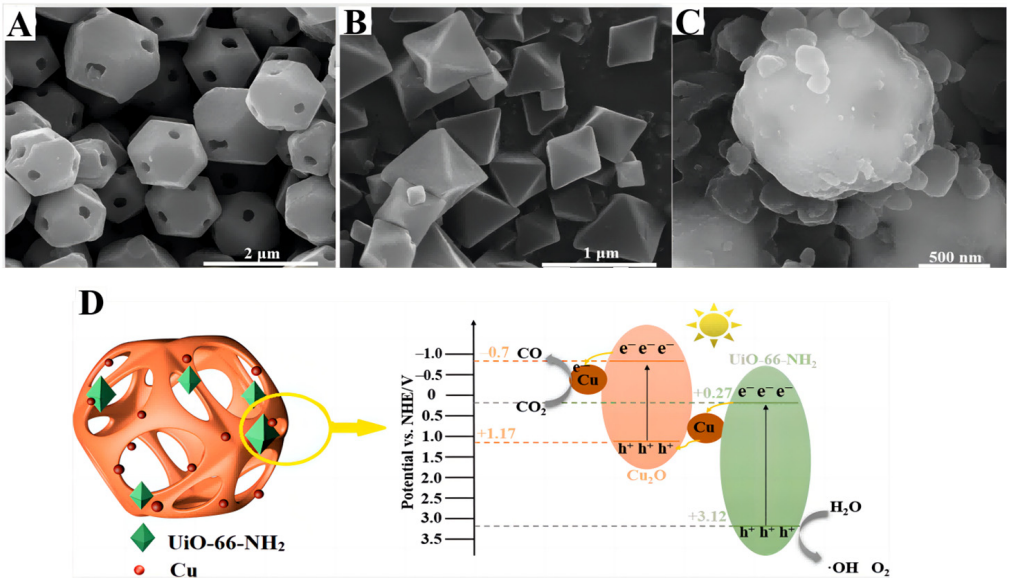


**Figure 18.** (**A**–**C**) SEM results of $Cu_2O$, UiO-66-$NH_2$ and U/C/Cu-0.39. (**D**) Illustration of the photocatalytic $CO_2$ reduction in U/C/Cu-0.39 [122].

### 3.4.3. Summary

In conclusion, photochemical methods offer the opportunity to modulate the persistence and selectivity of Cu-based catalysts photoreduction to value-added compounds.

The most recent photocatalytic $CO_2$ reduction outcomes of Cu-based materials are listed in Table 4.

**Table 4.** Summary of the recent results on the photoreduction of $CO_2$ by $Cu_2O$-based materials.

| Type of Enhancement | Photocatalyst | Description | Conditions (Lamp, Cutoff Filter) | Product Yield/ $\mu mol \cdot g^{-1} \cdot h^{-1}$ | Refs. |
|---|---|---|---|---|---|
| Heterojunction S-scheme | $Cu_2O$/CNPs | Coal-based carbon nanoparticles, multilayer graphene lattice structure | 300 W Xe | $CH_3OH$ 24.86 | [120] |
| | g-$C_3N_4$ foam/$Cu_2O$ QDs | 3D g-$C_3N_4$ foam, 0D $Cu_2O$ QDs | 300 W high-pressure Hg | CO 8.182 | [123] |
| | $Cu_2O$/rGO | Rhombic dodecahedra | 300 W Xe 420 nm | $CH_3OH$ 17.77 | [117] |
| | Ag/$Cu_2O$@rGO | Octahedral $Cu_2O$ | 300 W Xe 380 nm | $CH_4$ 82.6 | [112] |
| Z-scheme | UiO-66-$NH_2$/$Cu_2O$/Cu | Octahedron UiO-66-$NH_2$ | 300 W Xe | CO 4.54 | [122] |
| p–n hetero-junction | $Mg(OH)_2$/CuO/$Cu_2O$ | Microwave-hydrothermal method | Liquid phase: two halogen lamps of 20W | $CH_3OH$ 6 HCHO 9 | [118] |
| | $Cu_2O$/$SnS_2$/$SnO_2$ | Hierarchical flower-like $SnS_2$/$SnO_2$ | 300 W Xe | CO 3.18 $CH_4$ 2.27 | [119] |
| 3DOM | 3D porous $Cu_2O$ | | 300 W Xe, 420nm | CO 13.4 nmol $cm^{-2}h^{-1}$ | [114] |

### *3.5. $CeO_2$-Based Photocatalysts*

Cerium oxide ($CeO_2$) has an octahedral face-centered cubic fluorite structure, in which the coordination numbers of Ce and O are 8 and 4. When reduced at a high temperature, it can be converted to nonstoichiometric $CeO_{2-x}$ ($0 < x < 0.5$). Notably, $CeO_{2-x}$ maintains a fluorite crystal structure and forms oxygen vacancies after losing a certain amount of oxygen. $CeO_{2-x}$ materials with different Ce/O ratios were also obtained in different conditions and it could be reconverted to $CeO_2$ again if it returned to an oxidizing environment. Because of the unique electrical structure, cerium oxide ($CeO_2$) is famous for the conversion sates between $Ce^{4+}$ and $Ce^{3+}$, which have been studied as oxygen storage catalytic materials and solid oxide full cells by many scholars [124,125]. In summary, $CeO_2$ is a rare-earth metal oxide with a good photochemical stability, low cost and environment friendly characteristics. It is an important n-type semiconductor with a wide bandgap, and credible photocatalysts have been designed to reduce $CO_2$ and degrade pollutants [126].

#### 3.5.1. Morphology Control

Yb-, Er-doped $CeO_2$ hollow nanotubes were synthesized [127] using silver nanowires coated with silica, and the products had a narrower band gap of 2.8 eV. The core–shell structured $CeO_2$ was converted into mesoporous hollow spheres by the Ostwald ripening method in the presence of urea and hydrogen peroxide [128]. $CeO_2$ nanocages can be fabricated by mixing $(NH_4)_2Ce(NO_3)_2$ with templates of $Cu_2O$ nanocubes [129], in which $Cu_2O$ is finally sacrificed. The photocatalytic results [130] indicated that $CeO_2$ nanocages exhibit higher activity than hollow spheres.

#### Preferentially Exposed Facets

It was found that molecular $CO_2$ can be distorted and participate in reactions at a low energy on the $CeO_2$ surface [131]. A p-type NiO material was designed to modify the rod-like $CeO_2$ nanostructure [132], allowing electrons and holes to migrate to opposite directions. They then operated the Mott–Schottky test, which showed a typical p–n junction. The presence of hexagon-shaped NiO plates broadened the range of light responses, which

can be verified in the UV-Vis absorption spectra. Graphene oxide (rGO) was introduced as a "network" of for photoreduction electron transportation (Figure 19A–C). The impedance can be seen in the EIS Nyquist plot, which shows that the $NiO/CeO_2/rGO$ achieved the minimum value. The HCHO production rate of the ultimate catalyst was 421 μmol $g^{-1}h^{-1}$ with the synergy of several favorable factors. It is worth mentioning that a range of in situ techniques have been used to detect oxygen vacancies, structural changes, free radicals and formate on the surface of $CeO_2$.

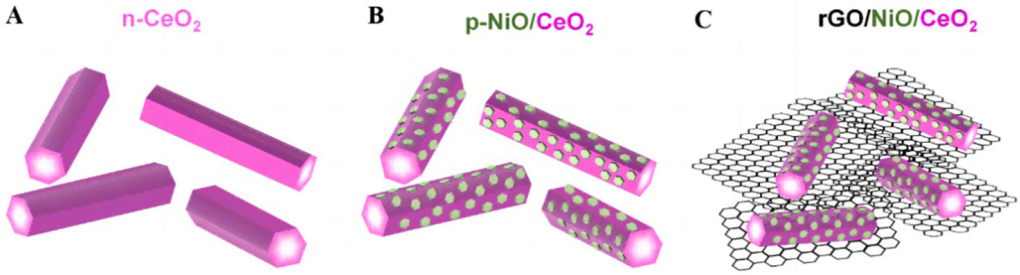


**Figure 19.** The structural diagrams of (**A**) n-$CeO_2$ nanorods, (**B**) p-$NiO/CeO_2$ composite and (**C**) $NiO/CeO_2/rGO$ hybrid composite [132].

Macroporous

Mesoporous N-doped $CeO_2$(NMCe), a relatively ordered intermediate structure with enhanced $CO_2$-capturing capability, was prepared without any convoluted procedures or expensive equipment [124]. In the Roman spectrum, the bands from 550 to 650 $cm^{-1}$, which are closely related to oxygen vacancy, were more salient than the MCe band. In addition, N-doped porous $CeO_2$ has a higher $CO_2$ absorption capacity than porous $CeO_2$. All the above results conformed to the photoluminescence spectrum (PL) analysis, and the reduction gross yield of CO and $CH_4$ was 3.5 times higher than that of OMCe.

With the help of a suitable crosslinked and pyrogenic solvent, doped $CeO_2$ was uniformly fixed on transparent polymers by the in situ polymerization pathway [133]. By increasing the Ca/Ce molar ratio (wt.% < 20%), no peaks relating to CaO were observed in the p-XRD of samples and the original diffraction peak intensity became more strident due to the foreign ion's minuscule radius ($Ca^{2+}$ 0.1 nm, $Ce^{4+}$ 0.184 nm). The specific surface areas of three catalysts ($CeO_2$, (20: 80) $CaO/CeO_2$ and $CaO/CeO_2$ NC-dispersed polymers as a whole) were 28.4, 58.3 and 224.7 $m^2$ $g^{-1}$, respectively, and heterojunction nanocomposites had the highest photocatalytic efficiency.

3DOM Structure Ce-Based Materials

Under the protection of poly alcohol, Zhang et al. [134] synthesized 3DOM $CeO_2$ that was loaded with Au–Pd alloys. 3DOM $CeO_2$ photocatalytic materials are expected to emerge in the field of $CO_2$ emission reduction, which could open up more possibilities for the development of super-catalysts.

3.5.2. Heterojunction

Researchers tried to combine $CeO_2$ with g-$C_3N_4$, which is popular for its energy bands and chemical stability. Through hard work, a three-dimensional porous g-$C_3N_4$(3DCN) was achieved, with the advantages of multi-channel structure. To accommodate more electrons and heighten the density of photoelectric currents, Zhao et al. [125] loaded Pt nanoparticles (5–6 nm) on $CeO_2$/3DCN using photodeposition techniques that require UV lamp radiation. The photoreduction rate gradually increased as the $CeO_2$ amount rose in the range of 15~45% and the yield rates of 4.69 and 3.03 $\mu mol \cdot h^{-1} \cdot g^{-1}$ for CO and $CH_4$ were achieved, respectively, after decorating with Pt crystalline grains.

Under mild reaction conditions, carbon-doped hexagonal boron nitride (h-BN), known as boron carbon nitride (BCN), can reduce more carbon dioxide after dispersing cerium oxides on it. In the $BCN/CeO_2$ heterostructure [135], the N-O-Ce bond was formed by

thermal precipitation method. It is of interest that the proportion of $Ce^{3+}/(Ce^{3+} + Ce^{4+})$ that influences electron transfer rate fluctuates with $CeO_2$-loading amount, and the yield of CO peaked on 30%$CeO_2$ (selected from 10% to 70%). When exposed to UV light, $CeO_2$ crystals could absorb more photons than visible light, whereas h-BN does not exhibit absorption in the UV range. The establishment of heterojunction expanded the effective wavelengths and improved the absorption capability in ultraviolet and visible light. The •OH species was detected by ESR analysis to identify the type of the heterostructure and the result of no newly generated •OH species was in accord with the II-scheme system.

#### 3.5.3. Summary

As a whole, the wider light harvesting range and longer separation time of charge pairs improved the photoreduction upshot. Overall, recent results on $CO_2$ photoreduction by $CeO_2$-based materials are presented in Table 5.

**Table 5.** Summary of the recent results on the photoreduction of $CO_2$ by $CeO_2$-based materials.

| Type of Enhancement | Photocatalyst | Description | Conditions (Lamp, Cutoff Filter) | Product Yield/ $\mu mol \cdot g^{-1} \cdot h^{-1}$ | Refs. |
|---|---|---|---|---|---|
| Heterojunction | modified $TiO_2$/rGO/$CeO_2$ | Sono-assisted, 0.75 wt% rGO and 1 wt% $CeO_2$ | UV light (a 15 W UV-C mercury) | $CH_3OH$ 106.83 $C_2H_5OH$ 45.17 | [53] |
| | S-C/$In_2O_3$-$CeO_2$ | S-doped, hollow hexagonal prisms with carbon coating | 300 W Xe | $CH_4$ 60.6 | [136] |
| | $CeO_2$/$Fe_3O_4$ | G-$C_3N_4$ QDs (CN QDs) $CeO_2$/$Fe_3O_4$ micro-Flowers (MFs) | UV-Vis light | CO 28.0 $CH_4$ 9.5 | [137] |
| | Ni/$CeO_2$ | Pure cubic fluorite structure $CeO_2$ | Xe 4.7 kW m-2 >500 °C | $H_2$ 6.53 CO 6.27 | [138] |
| | $CeO_2$@$Ti_3C_2TX$ | Layered $Ti_3C_2TX$ nanosheets, high-density $CeO_2$ | 300 W Xe | $CH_3OH$ 76.2 $C_2H_5OH$ 33.7 | [139] |
| Z-scheme | CoAl-LDH/$CeO_2$ | $CeO_2$ and RGO on the flower-like CoAl-LDHs | ultraviolet (UV) light (200 W) | CO 5.5 | [140] |
| p-n hetero-junction | NiO/$CeO_2$/rGO | $CeO_2$ nanorods, hexagon-shaped NiO plates | 300 W Xe | HCHO 421.09 | [132] |
| Ternary composites | N-$TiO_2$/$CeO_2$/CuO | N-doped $TiO_2$ | 2 Xe lamps (20 W each) | HCOOH 33 | [141] |
| Ion doping | Fe-Ni@$CeO_2$ | Spherical Fe and hexagonal Ni-doped $CeO_2$ nanorods | 20 W white LED | $CH_3OH$ 293.29 | [142] |

## 4. Other 3DOM Materials

In order to introduce advanced porous structures to slow the self-aggregation of quantum dots, Wang et al. [143] devised 3DOM N-doped carbon (NC) to support CdS and ZnO QDs (Figure 20). They filled the interspace in an ordered PS microsphere template and then employed a pyrolytic treatment and in situ growth methods. Compared to bulky CdS, the 3DOM compounds have a larger cathodic current density and enhanced light harvesting, bearing a satisfactory carbon monoxide yield of 5210 μmol $g^{-1}$ $h^{-1}$. A three-dimensional $SnO_2$ inverse opal structure was synthesized as gas sensors, soot oxidation catalyst and photoanode. The 3DOM $BiVO_4$/$SnO_2$ heterostructure was obtained by adding a $BiVO_4$ precursor to fill the space between $SnO_2$ skeleton and periodic PS template. The compatibility of energy states with $SnO_2$ significantly reduced their photoluminescence intensity. Meanwhile, Au nanoparticles enhanced the slow photon effect, which in turn increased the incident light utilization efficiency.

Moreover, some photoreduction results on 3DOM materials are listed in Table 6. From the above analysis, we can infer the great potential of macroporous materials for further development in the field of photocatalysis.

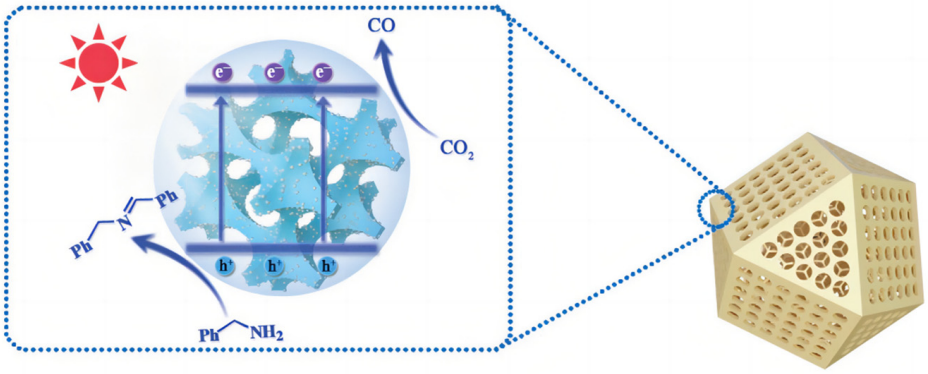


**Figure 20.** Proposed mechanism for the photocatalytic $CO_2$ reduction on 3DOM CdS QD/NC. Schematic illustration of the photocatalytic $CO_2$ reduction coupled with selective arylamine oxidation reaction system [143].

**Table 6.** Summary of the recent results on the photoreduction of $CO_2$ and $H_2O$ by 3DOM materials.

| Type of Enhancement | Photocatalyst | Conditions (Lamp, Cutoff Filter) | Product Yield/ $\mu mol \cdot g^{-1} \cdot h^{-1}$ | Refs. |
|---|---|---|---|---|
| Heterojunction | 3DOM Au-$CsPbBr_3$ | 300 W Xe 420 nm | CO 12.6 $CH_4$ 2.1 | [82] |
| | 3DOM CdS QDs/N-doped carbon | visible light irradiation, acetonitrile solution | CO 5210 | [143] |
| Water splitting to produce $H_2$ | CdS/Au/3DOM-$SrTiO_3$ | 300 W Xe 420 nm | $5.39 \times 10^3$ | [144] |
| | 3DOM Pt/ZnS@ZnO | 300 W Xe | 87.6 | [145] |
| | $TiO_2$-Au-CdS | 34 $mW/cm^2$ UV light, 158 $mW/cm^2$ visible light | $1.81 \times 10^3$ | [146] |

## 5. Conclusions

The photoconversion of $CO_2$ into solar fuels seems to curb greenhouse effect and resolve the energy crisis. In this review, the major research progresses of different metal oxide materials on solar-light-driven $CO_2$ conversion to fuels were carefully summarized. $TiO_2$, $WO_3$, ZnO, $Cu_2O$ and $CeO_2$ are the most common materials for photocatalysts among the numerous semiconductors. Even though considerable progress has been achieved, creating superb catalysts still presents several challenges. Researchers have presented treatment options to boost catalytic activity after apprehending the fundamental principles of objective reactions.

The main formulas for designing photocatalysts are as follows.

1. Absorb more photons to produce excitons.
2. Improve the migration efficiency of charge carriers.
3. Reduce the recombination rate of electron–hole pairs.
4. Uplift the absorption capacity of $CO_2$.

In terms of material selection, it is wise to choose metal oxides as one of the active components because of their relatively suitable *E*g and CB bands. From the perspective of morphology, compared with the solid and regular morphology, the structure of hollow ordered pores can promote the absorption of reactants and the desorption of products. A larger contact area between the catalyst and reactants and more active sites for the reaction can be provided. From the point of view of light absorption, the CB or VB positions can be adjusted after ion doping, which affects *E*g and influences the position of spectral absorption; the slow photon effect in the 3DOM structure can also improve the light utilization. As for charge separation efficiency, it can be promoted at the interface of the heterojunction, and photonic crystals can also improve their separation

efficiency by shortening the distance of charge movement to the interface. Numerous attempts have been made in the synthesis of metal oxide photocatalysts, which can yield CO, $CH_4$, HCHO, HCOOH, $CH_3OH$ and $C_2H_5OH$. However, it remains a great challenge for current photocatalysts to satisfy actual industrial production demands. The efficiency and selectivity for target products cannot meet the requirements for industrial and commercial implementation.

To sum up, the migration–separation efficiency of photoinduced pairs is important to improve the catalytic activity. Scholars should concentrate on the multiple advantages of photonic crystals to design catalysts with better performance based on them. This review provided a wealth of experience and ideas for the exploitation of photocatalyst material selection, morphology control and active site design. There is still a considerable work to conduct in converting $CO_2$ from solar energy to fuel, and we believe more significant breakthroughs can be achieved regarding the efficiency, mechanism and durability of the photocatalyst.

**Funding:** This research was funded by the National Natural Science Foundation of China (21972166, 22208373), Beijing Natural Science Foundation (2202045), the Technology Development Program of SINOPEC, China (Grant No. 321101) and National Key Research and Development Program of China (2019YFC1907600).

**Institutional Review Board Statement:** Not applicable.

**Informed Consent Statement:** Not applicable.

**Data Availability Statement:** Not applicable.

**Conflicts of Interest:** The authors declare no conflict of interest.

## References

1. Hou, Y.L.; Wang, Q.W.; Tan, T. Prediction of Carbon Dioxide Emissions in China Using Shallow Learning with Cross Validation. *Energies* **2022**, *15*, 8642. [CrossRef]
2. Xu, X.; Liao, M. Prediction of Carbon Emissions in China's Power Industry Based on the Mixed-Data Sampling (MIDAS) Regression Model. *Atmosphere* **2022**, *13*, 423. [CrossRef]
3. Fu, S.; Zhang, B.; Hu, H.; Zhang, Y.; Bi, Y. ZnO nanowire arrays decorated with PtO nanowires for efficient solar water splitting. *Catal. Sci. Technol.* **2018**, *8*, 2789–2793. [CrossRef]
4. Xu, Y.; Han, J.; Luo, Y.; Liu, Y.; Ding, J.; Zhou, Z.; Liu, C.; Zou, M.; Lan, J.; Nan, C.-w.; et al. Enhanced $CO_2$ Reduction Performance of BiCuSeO-Based Hybrid Catalysts by Synergetic Photo-Thermoelectric Effect. *Adv. Funct. Mater.* **2021**, *31*, 2105001. [CrossRef]
5. Tang, R.F.; Wang, H.; Dong, X.A.; Zhang, S.H.; Zhang, L.L.; Dong, F. A ball milling method for highly dispersed Ni atoms on g-$C_3N_4$ to boost $CO_2$ photoreduction. *J. Colloid Interface Sci.* **2023**, *630*, 290–300. [CrossRef]
6. Shen, H.; Peppel, T.; Stunk, J.; Sun, Z. Photocatalytic Reduction of $CO_2$ by Metal-Free-Based Materials: Recent Advances and Future Perspective. *Solar Rrl* **2020**, *4*, 1900546. [CrossRef]
7. Irfan, S.; Khan, S.B.; Lam, S.S.; Ong, H.C.; Din, M.A.U.; Dong, F.; Chen, D.L. Removal of persistent acetophenone from industrial waste-water via bismuth ferrite nanostructures. *Chemosphere* **2022**, *302*, 134750. [CrossRef]
8. Padervand, M.; Ghasemi, S.; Hajiahmadi, S.; Rhimi, B.; Nejad, Z.G.; Karima, S.; Shahsavari, Z.; Wang, C. Multifunctional Ag/AgCl/$ZnTiO_3$ structures as highly efficient photocatalysts for the removal of nitrophenols, $CO_2$ photoreduction, biomedical waste treatment, and bacteria inactivation. *Appl. Catal. A* **2022**, *643*, 118794. [CrossRef]
9. Padervand, M.; Rhimi, B.; Wang, C. One-pot synthesis of novel ternary $Fe_3N/Fe_2O_3/C_3N_4$ photocatalyst for efficient removal of rhodamine B and $CO_2$ reduction. *J. Alloys Compd.* **2021**, *852*, 156955. [CrossRef]
10. Padervand, M.; Ghasemi, S.; Hajiahmadi, S.; Wang, C. $K_4Nb_6O_{17}/Fe_3N/\alpha$-$Fe_2O_3/C_3N_4$ as an enhanced visible light-driven quaternary photocatalyst for acetamiprid photodegradation, $CO_2$ reduction, and cancer cells treatment. *Appl. Surf. Sci.* **2021**, *544*, 148939. [CrossRef]
11. Tran, D.P.H.; Pham, M.T.; Bui, X.T.; Wang, Y.F.; You, S.J. $CeO_2$ as a photocatalytic material for $CO_2$ conversion: A review. *Sol. Energy* **2022**, *240*, 443–466. [CrossRef]
12. Ali, S.; Lee, J.; Kim, H.; Hwang, Y.; Razzaq, A.; Jung, J.-W.; Cho, C.-H.; In, S.-I. Sustained, photocatalytic $CO_2$ reduction to $CH_4$ in a continuous flow reactor by earth-abundant materials: Reduced titania-$Cu_2O$ Z-scheme heterostructures. *Appl. Catal. B* **2020**, *279*, 119344. [CrossRef]
13. Li, R.; Luan, Q.; Dong, C.; Dong, W.; Tang, W.; Wang, G.; Lu, Y. Light-facilitated structure reconstruction on self-optimized photocatalyst $TiO_2$@BiOCl for selectively efficient conversion of $CO_2$ to $CH_4$. *Appl. Catal. B.* **2021**, *286*, 119832. [CrossRef]

14. Jiao, W.Y.; Xie, Y.; He, F.; Wang, K.Y.; Ling, Y.; Hu, Y.Y.; Wang, J.L.; Ye, H.; Wu, J.; Hou, Y. A visible light-response flower-like La-doped BiOBr nanosheets with enhanced performance for photoreducing $CO_2$ to $CH_3OH$. *Chem. Eng. J.* **2021**, *418*, 129286. [CrossRef]
15. Luévano, H.E.; Torres, M.L.M.; Fernández, T.A. Ternary ZnO/CuO/Zeolite composite obtained from volcanic ash for photocatalytic $CO_2$ reduction and $H_2O$ decomposition. *J. Phys. Chem. Solids* **2021**, *151*, 109917. [CrossRef]
16. Liu, L.; Wang, S.; Huang, H.; Zhang, Y.; Ma, T. Surface sites engineering on semiconductors to boost photocatalytic $CO_2$ reduction. *Nano Energy* **2020**, *75*, 126799. [CrossRef]
17. Zhang, D.Q.; Mao, B.D.; Li, D.; Liu, Y.H.; Li, F.H.; Dong, W.X.; Jiang, T.Y.; Shi, W.D. 0D/2D Z-scheme heterojunctions of Zn-$AgIn_5S_8$ QDs/alpha-$Fe_2O_3$ nanosheets for efficient visible-light-driven hydrogen production. *Chem. Eng. J.* **2021**, *417*, 128275. [CrossRef]
18. Nasir, M.S.; Yang, G.R.; Ayub, I.; Wang, S.L.; Yan, W. In situ decoration of g-$C_3N_4$ quantum dots on 1D branched $TiO_2$ loaded with plasmonic Au nanoparticles and improved the photocatalytic hydrogen evolution activity. *Appl. Surf. Sci.* **2020**, *519*, 146208. [CrossRef]
19. Li, M.; Ma, L.N.; Luo, L.; Liu, Y.G.; Xu, M.; Zhou, H.; Wang, Y.; Li, Z.H.; Kong, X.G.; Duan, H.H. Efficient photocatalytic epoxidation of styrene over a quantum-sized SnO(2)on carbon nitride as a heterostructured catalyst. *Appl. Catal. B.* **2022**, *309*, 121268. [CrossRef]
20. Xiong, H.; Dong, Y.; Liu, D.; Long, R.; Kong, T.; Xiong, Y. Recent Advances in Porous Materials for Photocatalytic $CO_2$ Reduction. *J. Phys. Chem. Lett.* **2022**, *13*, 1272–1282. [CrossRef]
21. Liu, J.; Zhao, H.; Wu, M.; Van der Schueren, B.; Li, Y.; Deparis, O.; Ye, J.; Ozin, G.A.; Hasan, T.; Su, B.L. Slow Photons for Photocatalysis and Photovoltaics. *Adv. Mater.* **2017**, *29*, 1605349. [CrossRef] [PubMed]
22. Zhao, H.; Hu, Z.; Liu, J.; Li, Y.; Wu, M.; Van Tendeloo, G.; Su, B.-L. Blue-edge slow photons promoting visible-light hydrogen production on gradient ternary 3DOM $TiO_2$-Au-CdS photonic crystals. *Nano Energy* **2018**, *47*, 266–274. [CrossRef]
23. Chen, J.I.L.; von Freymann, G.; Choi, S.Y.; Kitaev, V.; Ozin, G.A. Amplified Photochemistry with Slow Photons. *Adv. Mater.* **2006**, *18*, 1915–1919. [CrossRef]
24. Wu, M.; Jin, J.; Liu, J.; Deng, Z.; Li, Y.; Deparis, O.; Su, B.-L. High photocatalytic activity enhancement of titania inverse opal films by slow photon effect induced strong light absorption. *J. Mater. Chem.* **2013**, *1*, 15491–15500. [CrossRef]
25. Wu, M.; Li, Y.; Deng, Z.; Su, B.L. Three-dimensionally ordered macroporous titania with structural and photonic effects for enhanced photocatalytic efficiency. *ChemSusChem* **2011**, *4*, 1481–1488. [CrossRef]
26. Li, J.F.; Zhong, C.Y.; Huang, J.R.; Chen, Y.; Wang, Z.; Liu, Z.Q. Carbon dots decorated three-dimensionally ordered macroporous bismuth-doped titanium dioxide with efficient charge separation for high performance photocatalysis. *J. Colloid Interface Sci.* **2019**, *553*, 758–767. [CrossRef] [PubMed]
27. He, H.K.; Zhong, M.J.; Konkolewicz, D.; Yacatto, K.; Rappold, T.; Sugar, G.; David, N.E.; Gelb, J.; Kotwal, N.; Merkle, A.; et al. Three-Dimensionally Ordered Macroporous Polymeric Materials by Colloidal Crystal Templating for Reversible $CO_2$ Capture. *Adv. Funct. Mater.* **2013**, *23*, 4720–4728. [CrossRef]
28. Wang, P.F.; Zhan, S.H. Shedding light on the role of interfacial chemical bond in heterojunction photocatalysis. *Nano Res.* **2022**, *15*, 10158–10170.
29. Li, X.; Yu, J.; Jaroniec, M. Hierarchical photocatalysts. *Chem. Soc. Rev.* **2016**, *45*, 2603–2636. [CrossRef]
30. Yan, X.W.; Wang, B.; Zhao, J.Z.; Liu, G.P.; Ji, M.X.; Zhang, X.L.; Chu, P.K.; Li, H.M.; Xia, J.X. Hierarchical columnar $ZnIn_2S_4$/$BiVO_4$ Z-scheme heterojunctions with carrier highway boost photocatalytic mineralization of antibiotics. *Chem. Eng. J.* **2023**, *452*, 139271. [CrossRef]
31. Ji, M.X.; Feng, J.; Zhao, J.Z.; Zhang, Y.; Wang, B.; Di, J.; Xu, X.Y.; Chen, Z.R.; Xia, J.X.; Li, H.M. Defect-Engineered $Bi_{24}O_{31}Cl_{10}$ Nanosheets for Photocatalytic $CO_2$ Reduction to CO br. *ACS Appl. Nano Mater.* **2022**, *5*, 17226–17233. [CrossRef]
32. Bai, S.; Zhang, N.; Gao, C.; Xiong, Y.J. Defect engineering in photocatalytic materials. *Nano Energy* **2018**, *53*, 296–336. [CrossRef]
33. Shown, I.; Samireddi, S.; Chang, Y.C.; Putikam, R.; Chang, P.H.; Sabbah, A.; Fu, F.Y.; Chen, W.F.; Wu, C.I.; Yu, T.Y.; et al. Carbon-doped $SnS_2$ nanostructure as a high-efficiency solar fuel catalyst under visible light. *Nat. Commun.* **2018**, *9*, 169. [CrossRef] [PubMed]
34. Wan, S.P.; Ou, M.; Wang, X.M.; Wang, Y.A.; Zeng, Y.Q.; Ding, J.; Zhang, S.L.; Zhong, Q. Facile fabrication of oxygen and carbon co-doped carbon nitride nanosheets for efficient visible light photocatalytic $H_2$ evolution and $CO_2$ reduction. *Dalton Trans.* **2019**, *48*, 12070–12079. [CrossRef]
35. Zhang, D.P.; Li, Y.X.; Li, Y.; Zhan, S.H. Towards single-atom photocatalysts for future carbon-neutral application. *Smartmat* **2022**, *3*, 417–446. [CrossRef]
36. Kim, A.; Debecker, D.P.; Devred, F.; Dubois, V.; Sanchez, C.; Sassoye, C. $CO_2$ methanation on Ru/$TiO_2$ catalysts: On the effect of mixing anatase and rutile $TiO_2$ supports. *Appl. Catal. B.* **2018**, *220*, 615–625. [CrossRef]
37. Yang, X.; Tan, F.; Wang, D.; Feng, Q.; Qiu, D.; Dang, D.; Wang, X. Entrapping Ru nanoparticles into $TiO_2$ nanotube: Insight into the confinement synergy on boosting pho-thermal $CO_2$ methanation activity. *Ceram. Int.* **2021**, *47*, 27316–27323. [CrossRef]
38. Kar, P.; Farsinezhad, S.; Mahdi, N.; Zhang, Y.; Obuekwe, U.; Sharma, H.; Shen, J.; Semagina, N.; Shankar, K. Enhanced $CH_4$ yield by photocatalytic $CO_2$ reduction using $TiO_2$ nanotube arrays grafted with Au, Ru, and ZnPd nanoparticles. *Nano Res.* **2016**, *9*, 3478–3493. [CrossRef]

39. Dong, C.Y.; Xing, M.Y.; Zhang, J.L. Double-cocatalysts promote charge separation efficiency in $CO_2$ photoreduction: Spatial location matters. *Mater. Horiz.* **2016**, *3*, 608–612. [CrossRef]
40. Ma, Y.J.; Tang, Q.; Sun, W.Y.; Yao, Z.Y.; Zhu, W.H.; Li, T.; Wang, J.Y. Assembling ultrafine $TiO_2$ nanoparticles on UiO-66 octahedrons to promote selective photocatalytic conversion of $CO_2$ to CH4 at a low concentration. *Appl. Catal. B.* **2020**, *270*, 118856. [CrossRef]
41. Hu, X.L.; Song, J.Y.; Luo, J.L.; Zhang, H.; Sun, Z.M.; Li, C.Q.; Zheng, S.L.; Liu, Q.X. Single-atomic Pt sites anchored on defective $TiO_2$ nanosheets as a superior photocatalyst for hydrogen evolution. *J. Energy Chem.* **2021**, *62*, 1–10. [CrossRef]
42. Yang, G.; Qiu, P.; Xiong, J.Y.; Zhu, X.T.; Cheng, G. Facilely anchoring $Cu_2O$ nanoparticles on mesoporous $TiO_2$ nanorods for enhanced photocatalytic $CO_2$ reduction through efficient charge transfer. *Chin. Chem. Lett.* **2022**, *33*, 3709–3712. [CrossRef]
43. Zalfani, M.; Hu, Z.Y.; Yu, W.B.; Mahdouani, M.; Bourguiga, R.; Wu, M.; Li, Y.; Van Tendeloo, G.; Djaoued, Y.; Su, B.L. $BiVO_4$/3DOM $TiO_2$ nanocomposites: Effect of $BiVO_4$ as highly efficient visible light sensitizer for highly improved visible light photocatalytic activity in the degradation of dye pollutants. *Appl. Catal. B.* **2017**, *205*, 121–132. [CrossRef]
44. Jiao, J.Q.; Wei, Y.C.; Zhao, Z.; Liu, J.; Li, J.M.; Duan, A.J.; Jiang, G.Y. Photocatalysts of 3D Ordered Macroporous $TiO_2$-Supported $CeO_2$ Nano layers: Design, Preparation, and Their Catalytic Performances for the Reduction of $CO_2$ with $H_2O$ under Simulated Solar Irradiation. *Ind. Eng. Chem. Res.* **2014**, *53*, 17345–17354. [CrossRef]
45. Wang, C.J.; Liu, X.; He, W.J.; Zhao, Y.L.; Wei, Y.C.; Xiong, J.; Liu, J.; Li, J.M.; Song, W.Y.; Zhang, X.; et al. All-solid-state Z-scheme photocatalysts of g-$C_3N_4$/Pt/macroporous-($TiO_2$@carbon) for selective boosting visible-light-driven conversion of $CO_2$ to $CH_4$. *J. Catal.* **2020**, *389*, 440–449. [CrossRef]
46. Wu, X.X.; Wang, C.J.; Wei, Y.C.; Xiong, J.; Zhao, Y.L.; Zhao, Z.; Liu, J.; Li, J.M. Multifunctional photocatalysts of Pt-decorated 3DOM perovskite-type $SrTiO_3$ with enhanced $CO_2$ adsorption and photoelectron enrichment for selective $CO_2$ reduction with $H_2O$ to $CH_4$. *J. Catal.* **2019**, *377*, 309–321. [CrossRef]
47. Li, Y.F.; Tang, J.J.; Wei, Y.C.; He, W.J.; Tang, Z.L.; Zhang, X.; Xiong, J.; Zhao, Z. The heterojunction between 3D ordered macroporous $TiO_2$ and $MoS_2$ nanosheets for enhancing visible-light driven $CO_2$ reduction. *J. $CO_2$ Util.* **2021**, *51*, 101648. [CrossRef]
48. Chen, C.; Wang, T.; Yan, K.; Liu, S.J.; Zhao, Y.; Li, B.X. Photocatalytic $CO_2$ reduction on Cu single atoms incorporated in ordered macroporous $TiO_2$ toward tunable products. *Inorg. Chem. Front.* **2022**, *9*, 4753–4767. [CrossRef]
49. Jiao, J.; Wei, Y.; Zhao, Y.; Zhao, Z.; Duan, A.; Liu, J.; Pang, Y.; Li, J.; Jiang, G.; Wang, Y. AuPd/3DOM-$TiO_2$ catalysts for photocatalytic reduction of $CO_2$: High efficient separation of photogenerated charge carriers. *Appl. Catal. B.* **2017**, *209*, 228–239. [CrossRef]
50. Zhao, H.; Liu, J.; Li, C.F.; Zhang, X.; Li, Y.; Hu, Z.Y.; Li, B.; Chen, Z.X.; Hu, J.G.; Su, B.L. Meso-Microporous Nanosheet-Constructed 3DOM Perovskites for Remarkable Photocatalytic Hydrogen Production. *Adv. Funct. Mater.* **2022**, *32*, 2112831. [CrossRef]
51. Tahir, M.S.; Manzoor, N.; Sagir, M.; Tahir, M.B.; Nawaz, T. Fabrication of $ZnFe_2O_4$ modified $TiO_2$ hybrid composites for photocatalytic reduction of $CO_2$ into methanol. *Fuel* **2021**, *285*, 119206. [CrossRef]
52. Qiu, B.C.; Xing, M.Y.; Zhang, J.L. Recent advances in three-dimensional graphene based materials for catalysis applications. *Chem. Soc. Rev.* **2018**, *47*, 2165–2216. [CrossRef] [PubMed]
53. Seeharaj, P.; Kongmun, P.; Paiplod, P.; Prakobmit, S.; Sriwong, C.; Kim-Lohsoontorn, P.; Vittayakorn, N. Ultrasonically-assisted surface modified $TiO_2$/rGO/$CeO_2$ heterojunction photocatalysts for conversion of $CO_2$ to methanol and ethanol. *Ultrason. Sonochem.* **2019**, *58*, 104657. [CrossRef] [PubMed]
54. Kumar, A.; Thakur, P.R.; Sharma, G.; Vo, D.N.; Naushad, M.; Tatarchuk, T.; Garcia-Penas, A.; Du, B.; Stadler, F.J. Accelerated charge transfer in well-designed S-scheme Fe@$TiO_2$/Boron carbon nitride heterostructures for high performance tetracycline removal and selective photo-reduction of $CO_2$ greenhouse gas into $CH_4$ fuel. *Chemosphere* **2022**, *287*, 132301. [CrossRef] [PubMed]
55. Zheng, L.X.; Teng, F.; Ye, X.Y.; Zheng, H.J.; Fang, X.S. Photo/Electrochemical Applications of Metal Sulfide/$TiO_2$ Heterostructures. *Adv. Energy Mater.* **2020**, *10*, 1902355. [CrossRef]
56. Hasanvandian, F.; Zehtab Salmasi, M.; Moradi, M.; Farshineh Saei, S.; Kakavandi, B.; Rahman Setayesh, S. Enhanced spatially coupling heterojunction assembled from CuCo2S4 yolk-shell hollow sphere capsulated by Bi-modified $TiO_2$ for highly efficient $CO_2$ photoreduction. *Chem. Eng. J.* **2022**, *444*, 136493. [CrossRef]
57. Zhang, H.; Wang, X.Y.; Li, N.; Xia, J.H.; Meng, Q.M.; Ding, J.C.; Lu, J. Synthesis and characterization of $TiO_2$/graphene oxide nanocomposites for photoreduction of heavy metal ions in reverse osmosis concentrate. *RSC Adv.* **2018**, *8*, 34241–34251. [CrossRef]
58. Mgolombane, M.; Bankole, O.M.; Ferg, E.E.; Ogunlaja, A.S. Construction of Co-doped $TiO_2$/rGO nanocomposites for high-performance photoreduction of $CO_2$ with $H_2O$: Comparison of theoretical binding energies and exploration of surface chemistry. *Mater. Chem. Phys.* **2021**, *268*, 124733. [CrossRef]
59. Lee, J.H.; Kim, S.-I.; Park, S.-M.; Kang, M. A p-n heterojunction NiS-sensitized $TiO_2$ photocatalytic system for efficient photoreduction of carbon dioxide to methane. *Ceram. Int.* **2017**, *43*, 1768–1774. [CrossRef]
60. Tahir, M.; Tahir, B.; Amin, N.A.S.; Zakaria, Z.Y. Photo-induced reduction of $CO_2$ to CO with hydrogen over plasmonic Ag-NPs/TiO 2 NWs core/shell hetero-junction under UV and visible light. *J. $CO_2$ Util.* **2017**, *18*, 250–260. [CrossRef]
61. Wang, X.; Jiang, Z.; Chen, H.; Wang, K.; Wang, X. Photocatalytic $CO_2$ reduction with water vapor to CO and $CH_4$ in a recirculation reactor by Ag-$Cu_2O$/$TiO_2$ Z-scheme heterostructures. *J. Alloys Compd.* **2022**, *896*, 163030. [CrossRef]
62. Wei, Y.C.; Jiao, J.Q.; Zhao, Z.; Zhong, W.J.; Li, J.M.; Liu, J.; Jiang, G.Y.; Duan, A.J. 3D ordered macroporous $TiO_2$-supported Pt@CdS core-shell nanoparticles: Design, synthesis and efficient photocatalytic conversion of $CO_2$ with water to methane. *J. Mater. Chem. A* **2015**, *3*, 11074–11085. [CrossRef]

63. He, W.J.; Wu, X.X.; Li, Y.F.; Xiong, J.; Tang, Z.L.; Wei, Y.C.; Zhao, Z.; Zhang, X.; Liu, J. Z-scheme heterojunction of $SnS_2$-decorated 3DOM-$SrTiO_3$ for selectively photocatalytic $CO_2$ reduction into $CH_4$. *Chin. Chem. Lett.* **2020**, *31*, 2774–2778. [CrossRef]
64. Baserga, A.; Russo, V.; Di Fonzo, F.; Bailini, A.; Cattaneo, D.; Casari, C.S.; Bassi, A.L.; Bottani, C.E. Nanostructured tungsten oxide with controlled properties: Synthesis and Raman characterization. *Thin Solid Films* **2007**, *515*, 6465–6469. [CrossRef]
65. Cheng, H.F.; Huang, B.B.; Liu, Y.Y.; Wang, Z.Y.; Qin, X.Y.; Zhang, X.Y.; Dai, Y. An anion exchange approach to $Bi_2WO_6$ hollow microspheres with efficient visible light photocatalytic reduction of $CO_2$ to methanol. *Chem. Commun.* **2012**, *48*, 9729–9731. [CrossRef]
66. Li, B.; Sun, L.; Bian, J.; Sun, N.; Sun, J.; Chen, L.; Li, Z.; Jing, L. Controlled synthesis of novel Z-scheme iron phthalocyanine/porous WO3 nanocomposites as efficient photocatalysts for $CO_2$ reduction. *Appl. Catal. B.* **2020**, *270*, 1188849. [CrossRef]
67. Wang, L.; Wang, Y.; Cheng, Y.; Liu, Z.; Guo, Q.; Minh Ngoc, H.; Zhao, Z. Hydrogen-treated mesoporous $WO_3$ as a reducing agent of $CO_2$ to fuels ($CH_4$ and $CH_3OH$) with enhanced photothermal catalytic performance. *J. Mater. Chem. A* **2016**, *4*, 5314–5322. [CrossRef]
68. Rong, R.C.; Wang, L.M. Synthesis of hierarchical hollow nest-like $WO_3$ micro/nanostructures with enhanced visible light-driven photocatalytic activity. *J. Alloys Compd.* **2021**, *850*, 156742. [CrossRef]
69. Hao, Z.C.; Liu, Z.F.; Li, Y.T.; Ruan, M.N.; Guo, Z.G. Enhanced photoelectrochemical performance of 2D core-shell $WO_3$/$CuWO_4$ uniform heterojunction via in situ synthesis and modification of Co-Pi co-catalyst. *Int. J. Hydrog. Energy* **2020**, *45*, 16550–16559. [CrossRef]
70. Ren, X.Z.; Wu, K.; Qin, Z.G.; Zhao, X.C.; Yang, H. The construction of type II heterojunction of $Bi_2WO_6$/BiOBr photocatalyst with improved photocatalytic performance. *J. Alloys Compd.* **2019**, *788*, 102–109. [CrossRef]
71. Ling, P.Q.; Zhu, J.C.; Wang, Z.Q.; Hu, J.; Zhu, J.F.; Yan, W.S.; Sun, Y.F.; Xie, Y. Ultrathin Ti-doped $WO_3$ nanosheets realizing selective photoreduction of $CO_2$ to $CH_3OH$. *Nanoscale* **2022**, *14*, 14023–14028. [CrossRef] [PubMed]
72. Zhang, H.Y.; Tian, W.J.; Li, Y.G.; Sun, H.Q.; Tade, M.O.; Wang, S.B. Heterostructured $WO_3$@$CoWO_4$ bilayer nanosheets for enhanced visible-light photo, electro and photoelectro-chemical oxidation of water. *J. Mater. Chem. A* **2018**, *6*, 6265–6272. [CrossRef]
73. Hu, Y.F.; Ping, X.C.; Zhang, Y.; Hao, L.; Liu, T.Y.; Zhao, Q.; Lu, Y.; Liu, J.Z. A nanotree-like $WO_3$ film with adjustable defect concentration and its photocatalytic activity. *Mater. Sci. Semicond. Process.* **2021**, *127*, 105737. [CrossRef]
74. Liang, L.; Li, X.D.; Sun, Y.F.; Tan, Y.L.; Jiao, X.C.; Ju, H.X.; Qi, Z.M.; Zhu, J.F.; Xie, Y. Infrared Light-Driven $CO_2$ Overall Splitting at Room Temperature. *Joule* **2018**, *2*, 1004–1016. [CrossRef]
75. Chen, X.Y.; Zhou, Y.; Liu, Q.; Li, Z.D.; Liu, J.G.; Zou, Z.G. Ultrathin, Single-Crystal $WO_3$ Nanosheets by Two-Dimensional Oriented Attachment toward Enhanced Photocatalystic Reduction of $CO_2$ into Hydrocarbon Fuels under Visible Light. *ACS Appl. Mater. Interfaces* **2012**, *4*, 3372–3377. [CrossRef]
76. Zhou, Y.; Zhang, Y.; Lin, M.; Long, J.; Zhang, Z.; Lin, H.; Wu, J.C.; Wang, X. Monolayered $Bi_2WO_6$ nanosheets mimicking heterojunction interface with open surfaces for photocatalysis. *Nat. Commun.* **2015**, *6*, 8340. [CrossRef]
77. Zhou, Y.; Tian, Z.P.; Zhao, Z.Y.; Liu, Q.; Kou, J.H.; Chen, X.Y.; Gao, J.; Yan, S.C.; Zou, Z.G. High-Yield Synthesis of Ultrathin and Uniform $Bi_2WO_6$ Square Nanoplates Benefitting from Photocatalytic Reduction of $CO_2$ into Renewable Hydrocarbon Fuel under Visible Light. *ACS Appl. Mater. Interfaces* **2011**, *3*, 3594–3601. [CrossRef]
78. Zhang, K.F.; Chen, H.X.; Liu, Y.X.; Deng, J.G.; Jing, L.; Rastegarpanah, A.L.; Pei, W.B.; Han, Z.; Dai, H.X. Two-dimensional $Bi_2W_xMo_{1\_x}O_6$ solid solution nanosheets for enhanced photocatalytic toluene oxidation to benzaldehyde. *Appl. Catal. B* **2022**, *315*, 121545. [CrossRef]
79. Chang, Y.; Yu, K.; Zhang, C.; Li, R.; Zhao, P.; Lou, L.-L.; Liu, S. Three-dimensionally ordered macroporous WO3 supported Ag3PO4 with enhanced photocatalytic activity and durability. *Appl. Catal. B.* **2015**, *176–177*, 363–373. [CrossRef]
80. Tang, Z.; Wang, C.; He, W.; Wei, Y.; Zhao, Z.; Liu, J. The Z-scheme g-$C_3N_4$/3DOM-$WO_3$ photocatalysts with enhanced activity for $CO_2$ photoreduction into CO. *Chin. Chem. Lett.* **2022**, *33*, 939–942. [CrossRef]
81. Xie, Z.; Xu, Y.; Li, D.; Chen, L.; Meng, S.; Jiang, D.; Chen, M. Construction of CuO quantum Dots/$WO_3$ nanosheets 0D/2D Z-scheme heterojunction with enhanced photocatalytic $CO_2$ reduction activity under visible-light. *J. Alloys Compd.* **2021**, *858*, 157668. [CrossRef]
82. Zhang, Y.; Shi, L.; Yuan, H.; Sun, X.; Li, X.; Duan, L.; Li, Q.; Huang, Z.; Ban, X.; Zhang, D. Construction of melamine foam–supported $WO_3$/$CsPbBr_3$ S–scheme heterojunction with rich oxygen vacancies for efficient and long–period $CO_2$ photoreduction in liquid–phase $H_2O$ environment. *Chem. Eng. J.* **2022**, *430*, 132820. [CrossRef]
83. Wang, H.; Zhang, L.; Wang, K.; Sun, X.; Wang, W. Enhanced photocatalytic $CO_2$ reduction to methane over $WO_3 \cdot 0.33H_2O$ via Mo doping. *Appl. Catal. B.* **2019**, *243*, 771–779. [CrossRef]
84. Zhu, Z.; Huang, W.R.; Chen, C.Y.; Wu, R.J. Preparation of Pd–Au/$TiO_2$–WO3 to enhance photoreduction of $CO_2$ to $CH_4$ and CO. *J. $CO_2$ Util.* **2018**, *28*, 247–254. [CrossRef]
85. Chen, P.; Du, T.; Jia, H.; Zhou, L.; Yue, Q.; Wang, H.; Wang, Y. A novel Bi2WO6/Si heterostructure photocatalyst with Fermi level shift in valence band realizes efficient reduction of $CO_2$ under visible light. *Appl. Surf. Sci.* **2022**, *585*, 152665. [CrossRef]
86. Sun, Y.; Han, Y.; Song, X.; Huang, B.; Ma, X.; Xing, R. CdS/$WO_3$ S-scheme heterojunction with improved photocatalytic $CO_2$ reduction activity. *J. Photochem. Photobiol. B* **2022**, *233*, 112480. [CrossRef]
87. Raza, A.; Shen, H.; Haidry, A.A.; Sun, L.; Liu, R.; Cui, S. Studies of Z-scheme $WO_3$-$TiO_2$/Cu2ZnSnS4 ternary nanocomposite with enhanced $CO_2$ photoreduction under visible light irradiation. *J. $CO_2$ Util.* **2020**, *37*, 260–271. [CrossRef]

88. Tahir, B.; Tahir, M.; Nawawi, M.G.M. Highly sTable 3D/2D $WO_3$/g-$C_3N_4$ Z-scheme heterojunction for stimulating photocatalytic $CO_2$ reduction by $H_2O$/$H_2$ to CO and $CH_4$ under visible light. *J. $CO_2$ Util.* **2020**, *41*, 101270. [CrossRef]
89. Gao, H.; Zhang, P.; Hu, J.; Pan, J.; Fan, J.; Shao, G. One-dimensional Z-scheme $TiO_2$/$WO_3$/Pt heterostructures for enhanced hydrogen generation. *Appl. Surf. Sci.* **2017**, *391*, 211–217. [CrossRef]
90. Mohamed, R.M.; Mkhalid, I.A.; Alhaddad, M.; Basaleh, A.; Alzahrani, K.A.; Ismail, A.A. Enhanced $CO_2$ photocatalytic conversion into $CH_3OH$ over visible-light-driven Pt nanoparticle-decorated mesoporous ZnO–ZnS S-scheme heterostructures. *Ceram. Int.* **2021**, *47*, 26779–26788. [CrossRef]
91. Cai, C.; Xu, Y.F.; Chen, H.Y.; Wang, X.D.; Kuang, D.B. Porous ZnO@ZnSe nanosheet array for photoelectrochemical reduction of $CO_2$. *Electrochim. Acta* **2018**, *274*, 298–305. [CrossRef]
92. Xia, W.W.; Mei, C.; Zeng, X.H.; Chang, S.; Wu, G.Q.; Shen, X.S. Mesoporous multi-shelled ZnO microspheres for the scattering layer of dye sensitized solar cell with a high efficiency. *Appl. Phys. Lett.* **2016**, *108*, 113902. [CrossRef]
93. Wang, P.; Yang, M.; Tang, S.; Li, Y.; Lin, X.; Zhang, H.; Zhu, Z.; Chen, F. Z-scheme heterojunctions composed of 3D graphene aerogel/g-$C_3N_4$ nanosheets/porous ZnO nanospheres for the efficient photocatalytic reduction of $CO_2$ with $H_2O$ under visible light irradiation. *J. Alloys Compd.* **2022**, *918*, 165607. [CrossRef]
94. Dong, Z.; Wu, Y.; Thirugnanam, N.; Li, G. Double Z-scheme ZnO/ZnS/g-$C_3N_4$ ternary structure for efficient photocatalytic $H_2$ production. *Appl. Surf. Sci.* **2018**, *430*, 293–300. [CrossRef]
95. Taraka, T.P.Y.; Gautam, A.; Jain, S.L.; Bojja, S.; Pal, U. Controlled addition of Cu/Zn in hierarchical CuO/ZnO p-n heterojunction photocatalyst for high photoreduction of $CO_2$ to MeOH. *J. $CO_2$ Util.* **2019**, *31*, 207–214. [CrossRef]
96. Chen, S.Q.; Yu, J.G.; Zhang, J. Enhanced photocatalytic $CO_2$ reduction activity of MOF-derived ZnO/NiO porous hollow spheres. *J. $CO_2$ Util.* **2018**, *24*, 548–554. [CrossRef]
97. Saravanan, R.; Agarwal, S.; Gupta, V.K.; Khan, M.M.; Gracia, F.; Mosquera, E.; Narayanan, V.; Stephen, A. Line defect $Ce^{3+}$ induced Ag/$CeO_2$/ZnO nanostructure for visible-light photocatalytic activity. *J. Photochem. Photobiol. A* **2018**, *353*, 499–506. [CrossRef]
98. Xu, K.; Liu, Z.; Qi, S.H.; Yin, Z.Z.; Deng, S.K.; Zhang, M.; Sun, Z.Q. The quaternary system of Ag2S/ZnS co-modified ZnO/$TiO_2$ nanotree arrays: Excellent photocatalysis and photoelectrochemistry performance. *Appl. Surf. Sci.* **2021**, *538*, 148044. [CrossRef]
99. Wang, Y.; Fan, G.; Wang, S.; Li, Y.; Guo, Y.; Luan, D.; Gu, X.; Lou, X.W. Implanting $CoO_x$ Clusters on Ordered Macroporous ZnO Nanoreactors for Efficient $CO_2$ Photoreduction. *Adv. Mater.* **2022**, *34*, 2204865. [CrossRef]
100. Tang, Z.; Zhu, F.; Zhou, J.; Chen, W.; Wang, K.; Liu, M.; Wang, N.; Li, N. Monolithic NF@ZnO/Au@ZIF-8 photocatalyst with strong photo-thermal-magnetic coupling and selective-breathing effects for boosted conversion of $CO_2$ to $CH_4$. *Appl. Catal. B.* **2022**, *309*, 121267. [CrossRef]
101. Xie, F.; Guo, J.-F.; Wang, H.-T.; Chang, N. Enhancing visible light photocatalytic activity by transformation of $Co^{3+}$/$Co^{2+}$ and formation of oxygen vacancies over rationally Co doped ZnO microspheres. *Colloids Surf. A* **2022**, *636*, 128257. [CrossRef]
102. Shi, C.; Zhang, L.; Shi, Z.; Ma, J.; Wang, Z. Cellulose template designed porous ZnO based catalysts with different valence copper for solar photocatalytic $CO_2$ conversion. *Ind. Crops Prod.* **2022**, *186*, 115223. [CrossRef]
103. Lin, L.-Y.; Liu, C.; Hsieh, T.-T. Efficient visible and NIR light-driven photocatalytic $CO_2$ reduction over defect-engineered ZnO/carbon dot hybrid and mechanistic insights. *J. Catal.* **2020**, *391*, 298–311. [CrossRef]
104. Zhang, F.; Li, Y.-H.; Qi, M.-Y.; Tang, Z.-R.; Xu, Y.-J. Boosting the activity and stability of Ag-$Cu_2O$/ZnO nanorods for photocatalytic $CO_2$ reduction. *Appl. Catal. B.* **2020**, *268*, 118380. [CrossRef]
105. Guo, Q.; Zhang, Q.; Wang, H.; Liu, Z.; Zhao, Z. Core-shell structured ZnO@Cu-Zn–Al layered double hydroxides with enhanced photocatalytic efficiency for $CO_2$ reduction. *Catal. Commun.* **2016**, *77*, 118–122. [CrossRef]
106. Zhang, P.P.; Zhou, Z.J.; Kou, D.X.; Wu, S.X. Perovskite Thin Film Solar Cells Based on Inorganic Hole Conducting Materials. *Int. J. Photoenergy* **2017**, *2017*, 6109092. [CrossRef]
107. Li, X.; Wang, Z.; Zhang, J.; Dai, K.; Fan, K.; Dawson, G. Branch-like $Cd_xZn_{1-x}Se$/Cu2O@Cu step-scheme heterojunction for $CO_2$ photoreduction. *Mater. Today Phys.* **2022**, *26*, 100729. [CrossRef]
108. Yao, S.; Sun, B.Q.; Zhang, P.; Tian, Z.Y.; Yin, H.Q.; Zhang, Z.M. Anchoring ultrafine $Cu_2O$ nanocluster on PCN for $CO_2$ photoreduction in water vapor with much improved stability. *Appl. Catal. B.* **2022**, *317*, 121702. [CrossRef]
109. Zhang, J.Z.; Shi, J.J.; Tao, S.; Wu, L.; Lu, J. $Cu_2O$/$Ti_3C_2$ MXene heterojunction photocatalysts for improved $CO_2$ photocatalytic reduction performance. *Appl. Surf. Sci.* **2021**, *542*, 148685. [CrossRef]
110. Zhang, N.; Zhang, Q.; Xu, C.; Li, Y.; Zhang, J.Y.; Wu, L.; Liu, Y.F.; Fang, Y.Z.; Liu, Z.F. Optional construction of $Cu_2O$@$Fe_2O_3$@CC architecture as a robust multifunctional photoelectronic catalyst for overall water splitting and $CO_2$ reduction. *Chem. Eng. J.* **2021**, *426*, 131192. [CrossRef]
111. Zhang, D.F.; Zhang, H.; Guo, L.; Zheng, K.; Han, X.D.; Zhang, Z. Delicate control of crystallographic facet-oriented $Cu_2O$ nanocrystals and the correlated adsorption ability. *J. Mater. Chem.* **2009**, *19*, 5220–5225. [CrossRef]
112. Tang, Z.; He, W.; Wang, Y.; Wei, Y.; Yu, X.; Xiong, J.; Wang, X.; Zhang, X.; Zhao, Z.; Liu, J. Ternary heterojunction in rGO-coated Ag/$Cu_2O$ catalysts for boosting selective photocatalytic $CO_2$ reduction into $CH_4$. *Appl. Catal. B.* **2022**, *311*, 121371. [CrossRef]
113. Singh, S.; Punia, R.; Pant, K.K.; Biswas, P. Effect of work-function and morphology of heterostructure components on $CO_2$ reduction photo-catalytic activity of $MoS_2$-$Cu_2O$ heterostructure. *Chem. Eng. J.* **2022**, *433*, 132709. [CrossRef]
114. Cui, L.; Hu, L.; Shen, Q.; Liu, X.; Jia, H.; Xue, J. Three-dimensional porous $Cu_2O$ with dendrite for efficient photocatalytic reduction of $CO_2$ under visible light. *Appl. Surf. Sci.* **2022**, *581*, 152343. [CrossRef]

115. Dong, Y.; Wang, Y.; Cai, T.; Kou, L.; Yang, G.; Yan, Z. Preparation and nitrogen-doping of three-dimensionally ordered macroporous $TiO_2$ with enhanced photocatalytic activity. *Ceram. Int.* **2014**, *40*, 11213–11219. [CrossRef]
116. Zheng, X.Z.; Han, J.; Fu, Y.; Deng, Y.; Liu, Y.Y.; Yang, Y.; Wang, T.; Zhang, L.W. Highly efficient $CO_2$ reduction on ordered porous Cu electrode derived from $Cu_2O$ inverse opals. *Nano Energy* **2018**, *48*, 93–100. [CrossRef]
117. Liu, S.H.; Lu, J.S.; Pu, Y.C.; Fan, H.C. Enhanced photoreduction of $CO_2$ into methanol by facet-dependent $Cu_2O$/reduce graphene oxide. *J. $CO_2$ Util.* **2019**, *33*, 171–178. [CrossRef]
118. Flores, F.M.; Luevano, H.E.; Torres, M.L.M.; Do, T.O. $CO_2$ adsorption and photocatalytic reduction over $Mg(OH)_{(2)}$/CuO/$Cu_2O$ under UV-Visible light to solar fuels. *Mater. Chem. Phys.* **2019**, *227*, 90–97. [CrossRef]
119. Ojha, N.; Bajpai, A.; Kumar, S. Enriched oxygen vacancies of $Cu_2O/SnS_2/SnO_2$ heterostructure for enhanced photocatalytic reduction of $CO_2$ by water and nitrogen fixation. *J. Colloid Interface Sci.* **2021**, *585*, 764–777. [CrossRef]
120. Dedong, Z.; Maimaiti, H.; Awati, A.; Yisilamu, G.; Fengchang, S.; Ming, W. Synthesis and photocatalytic $CO_2$ reduction performance of $Cu_2O$/Coal-based carbon nanoparticle composites. *Chem. Phys. Lett.* **2018**, *700*, 27–35. [CrossRef]
121. Shi, H.N.; Wang, H.Z.; Zhou, Y.C.; Li, J.H.; Zhai, P.L.; Li, X.Y.; Gurzadyan, G.G.; Hou, J.G.; Yang, H.; Guo, X.W. Atomically Dispersed Indium-Copper Dual-Metal Active Sites Promoting C-C Coupling for $CO_2$ Photoreduction to Ethanol. *Angew. Chem. Int. Ed.* **2022**, *61*, e202208904. [CrossRef] [PubMed]
122. Zhao, X.; Sun, L.; Jin, X.; Xu, M.; Yin, S.; Li, J.; Li, X.; Shen, D.; Yan, Y.; Huo, P. Cu media constructed Z-scheme heterojunction of UiO-66-$NH_2$/$Cu_2O$/Cu for enhanced photocatalytic induction of $CO_2$. *Appl. Surf. Sci.* **2021**, *545*, 148967. [CrossRef]
123. Sun, Z.; Fang, W.; Zhao, L.; Chen, H.; He, X.; Li, W.; Tian, P.; Huang, Z. g-$C_3N_4$ foam/$Cu_2O$ QDs with excellent $CO_2$ adsorption and synergistic catalytic effect for photocatalytic $CO_2$ reduction. *Environ. Int.* **2019**, *130*, 104898. [CrossRef] [PubMed]
124. Shen, Z.; Xia, Q.; Li, Y.; Yin, C.; Ge, Z.; Li, X.; Wang, Y. Adsorption-enhanced nitrogen-doped mesoporous $CeO_2$ as an efficient visible-light-driven catalyst for $CO_2$ photoreduction. *J. $CO_2$ Util.* **2020**, *39*, 101176. [CrossRef]
125. Zhao, X.; Guan, J.; Li, J.; Li, X.; Wang, H.; Huo, P.; Yan, Y. $CeO_2$/3D g-$C_3N_4$ heterojunction deposited with Pt cocatalyst for enhanced photocatalytic $CO_2$ reduction. *Appl. Surf. Sci.* **2021**, *537*, 147891. [CrossRef]
126. Feng, Y.; Ma, P.J.; Wang, Z.W.; Shi, Y.J.; Wang, Z.H.; Peng, Y.; Jing, L.; Liu, Y.X.; Yu, X.H.; Wang, X.; et al. Synergistic Effect of Reactive Oxygen Species in Photothermocatalytic Removal of VOCs from Cooking Oil Fumes over Pt/$CeO_2$/$TiO_2$. *Environ. Sci. Technol.* **2022**, *56*, 17341–17351. [CrossRef]
127. Zhao, R.F.; Huan, L.; Gu, P.; Guo, R.; Chen, M.; Diao, G.W. Yb,Er-doped $CeO_2$ nanotubes as an assistant layer for photoconversion-enhanced dye-sensitized solar cells. *J. Power Sources* **2016**, *331*, 527–534. [CrossRef]
128. Yang, Z.J.; Wei, J.J.; Yang, H.; Liu, L.X.; Liang, H.; Yang, Y.Z. Mesoporous $CeO_2$ Hollow Spheres Prepared by Ostwald Ripening and Their Environmental Applications. *Eur. J. Inorg. Chem.* **2010**, *2010*, 3354–3359. [CrossRef]
129. Ramani, S.; Sarkar, S.; Vemuri, V.; Peter, S.C. Chemically designed $CeO_2$ nanoboxes boost the catalytic activity of Pt nanoparticles toward electro-oxidation of formic acid. *J. Mater. Chem. A* **2017**, *5*, 11572–11576. [CrossRef]
130. Fang, S.; Xin, Y.; Ge, L.; Han, C.; Qiu, P.; Wu, L. Facile synthesis of $CeO_2$ hollow structures with controllable morphology by template-engaged etching of $Cu_2O$ and their visible light photocatalytic performance. *Appl. Catal. B.* **2015**, *179*, 458–467. [CrossRef]
131. Kumari, N.; Haider, M.A.; Agarwal, M.; Sinha, N.; Basu, S. Role of Reduced $CeO_2$(110) Surface for $CO_2$ Reduction to CO and Methanol. *J. Phys. Chem. C* **2016**, *120*, 16626–16635. [CrossRef]
132. Park, H.R.; Pawar, A.U.; Pal, U.; Zhang, T.; Kang, Y.S. Enhanced solar photoreduction of $CO_2$ to liquid fuel over rGO grafted NiO-$CeO_2$ heterostructure nanocomposite. *Nano Energy* **2021**, *79*, 105483. [CrossRef]
133. Asu, S.P.; Sompalli, N.K.; Kuppusamy, S.; Mohan, A.M.; Deivasigamani, P. CaO/$CeO_2$ nanocomposite dispersed macro-/meso-porous polymer monoliths as new generation visible light heterogeneous photocatalysts. *Mater. Today Sustain.* **2022**, *19*, 2317–2589. [CrossRef]
134. Zhang, X.; Liu, Y.X.; Deng, J.G.; Yu, X.H.; Han, Z.; Zhang, K.F.; Dai, H.X. Alloying of gold with palladium: An effective strategy to improve catalytic stability and chlorine-tolerance of the 3DOM $CeO_2$ -supported catalysts in trichloroethylene combustion. *Appl. Catal. B.* **2019**, *257*, 117879. [CrossRef]
135. Mei, Y.; Yuan, N.; Liu, Y.; Zhang, X.; Lin, B.; Zhou, Y. Boron Carbon Nitride Semiconductor Modified with $CeO_2$ for Photocatalytic Reduction of $CO_2$ with $H_2O$: Comparative Study. *Carbon Capture Sci. Technol.* **2021**, *1*, 100016. [CrossRef]
136. Wang, Q.; Chen, Y.; Liu, X.; Li, L.; Du, L.; Tian, G. Sulfur doped $In_2O_3$-$CeO_2$ hollow hexagonal prisms with carbon coating for efficient photocatalytic $CO_2$ reduction. *Chem. Eng. J. Chem. Eng. J.* **2021**, *421*, 129968. [CrossRef]
137. Wei, Y.; Li, X.; Zhang, Y.; Yan, Y.; Huo, P.; Wang, H. G-$C_3N_4$ quantum dots and Au nano particles co-modified $CeO_2$/$Fe_3O_4$ micro-flowers photocatalyst for enhanced $CO_2$ photoreduction. *Renew. Energy* **2021**, *179*, 756–765. [CrossRef]
138. Zhang, Q.; Mao, M.; Li, Y.; Yang, Y.; Huang, H.; Jiang, Z.; Hu, Q.; Wu, S.; Zhao, X. Novel photoactivation promoted light-driven $CO_2$ reduction by CH4 on Ni/$CeO_2$ nanocomposite with high light-to-fuel efficiency and enhanced stability. *Appl. Catal. B.* **2018**, *239*, 555–564. [CrossRef]
139. Zhang, S.; Xiong, W.; Long, J.; Si, Y.; Xu, Y.; Yang, L.; Zou, J.; Dai, W.; Luo, X.; Luo, S. High-throughput lateral and basal interface in $CeO_2$@$Ti_3C_2T_X$: Reverse and synergistic migration of carrier for enhanced photocatalytic $CO_2$ reduction. *J. Colloid Interface Sci.* **2022**, *615*, 716–724. [CrossRef] [PubMed]
140. Li, Z.; Liu, Z.; Li, Y.; Wang, Q. Flower-like CoAl layered double hydroxides modified with $CeO_2$ and RGO as efficient photocatalyst towards $CO_2$ reduction. *J. Alloys Compd.* **2021**, *881*, 160650. [CrossRef]

141. Ibarra-Rodriguez, L.I.; Pantoja-Espinoza, J.C.; Luévano-Hipólito, E.; Garay-Rodríguez, L.F.; López-Ortiz, A.; Torres-Martínez, L.M.; Collins-Martínez, V.H. Formic acid and hydrogen generation from the photocatalytic reduction of $CO_2$ on visible light activated N-$TiO_2$/$CeO_2$/CuO composites. *J. Photochem. Photobiol. A* **2022**, *11*, 100125. [CrossRef]
142. Prajapati, P.K.; Malik, A.; Nandal, N.; Pandita, S.; Singh, R.; Bhandari, S.; Saran, S.; Jain, S.L. Morphology controlled Fe and Ni-doped $CeO_2$ nanorods as an excellent heterojunction photocatalyst for $CO_2$ reduction. *Appl. Surf. Sci.* **2022**, *588*, 152912. [CrossRef]
143. Wang, F.; Hou, T.; Zhao, X.; Yao, W.; Fang, R.; Shen, K.; Li, Y. Ordered Macroporous Carbonous Frameworks Implanted with CdS Quantum Dots for Efficient Photocatalytic $CO_2$ Reduction. *Adv. Mater.* **2021**, *33*, e2102690. [CrossRef] [PubMed]
144. Chang, Y.; Yu, K.; Zhang, C.; Yang, Z.; Feng, Y.; Hao, H.; Jiang, Y.; Lou, L.-L.; Zhou, W.; Liu, S. Ternary CdS/Au/3DOM-$SrTiO_3$ composites with synergistic enhancement for hydrogen production from visible-light photocatalytic water splitting. *Appl. Catal. B.* **2017**, *215*, 74–84. [CrossRef]
145. Ji, X.; Xu, H.; Liang, S.; Gan, L.; Zhang, R.; Wang, X. 3D ordered macroporous Pt/ZnS@ZnO core-shell heterostructure for highly effective photocatalytic hydrogen evolution. *Int. J. Hydrog. Energy* **2022**, *47*, 17640–17649. [CrossRef]
146. Zhao, H.; Wu, M.; Liu, J.; Deng, Z.; Li, Y.; Su, B.-L. Synergistic promotion of solar-driven $H_2$ generation by three-dimensionally ordered macroporous structured $TiO_2$-Au-CdS ternary photocatalyst. *Appl. Catal. B.* **2016**, *184*, 182–190. [CrossRef]